# Formation of vascular-like structures using a chemotaxis-driven multiphase model

Georgina al-Badri [a,b,*], James B. Phillips [b,d], Rebecca J. Shipley [b,c], Nicholas C. Ovenden [a,b]

[a] *Department of Mathematics, University College London, London, UK*
[b] *Centre for Nerve Engineering, University College London, London, UK*
[c] *Department of Mechanical Engineering, University College London, London, UK*
[d] *Department of Pharmacology, University College London, London, UK*

## ARTICLE INFO

## ABSTRACT

We propose a continuum model for pattern formation, based on the multiphase model framework, to explore *in vitro* cell patterning within an extracellular matrix (ECM). We demonstrate that, within this framework, chemotaxis-driven cell migration can lead to the formation of cell clusters and vascular-like structures in 1D and 2D respectively. The influence on pattern formation of additional mechanisms commonly included in multiphase tissue models, including cell-matrix traction, contact inhibition, and cell–cell aggregation, are also investigated. Using sensitivity analysis, the relative impact of each model parameter on the simulation outcomes is assessed to identify the key parameters involved. Chemoattractant–matrix binding is further included, motivated by previous experimental studies, and found to reduce the spatial scale of patterning to within a biologically plausible range for capillary structures. Key findings from the in-depth parameter analysis of the 1D models, both with and without chemoattractant–matrix binding, are demonstrated to translate well to the 2D model, obtaining vascular-like cell patterning for multiple parameter regimes. Overall, we demonstrate a biologically-motivated multiphase model capable of generating long-term pattern formation on a biologically plausible spatial scale both in 1D and 2D, with applications for modelling *in vitro* vascular network formation.

## 1. Introduction

*In vitro* vascularisation of 3D engineered tissues is required for a range of applications, including *in vitro* models of development and disease e.g. vascularised tumours [1], and to support the rapid development of blood supply to engineered tissues implanted *in vivo*, e.g. in a thick skin graft [2,3]. Development of new strategies to fabricate prevascularised engineered tissues is ongoing, and is commonly described as one of the key challenges facing clinical application [4–7]. As engineered tissues are a complex combination of material properties and cell types, fabricated under a wide range of culture conditions, understanding the cell-level mechanisms behind *in vitro* vascular network formation and the interactions between network-forming endothelial cells (ECs) and other therapeutic cell types is essential to inform fabrication techniques.

Mathematical modelling of cell patterning, including of *in vitro* vascular network formation, offers a valuable tool to aid in the identification of the key cues and mechanisms involved [8], and to enable *in silico* trial and error of experimental conditions [9]. Where individual cell cues and mechanisms are difficult to isolate experimentally,

mathematical modelling offers the opportunity to probe the individual influence of each mechanism. Furthermore, computational techniques such as sensitivity analysis offer a powerful and cost-effective way to assess the relative importance of cell mechanisms and experimental conditions.

A first step to using simulation to guide experimental methods is to select a suitable mathematical framework that is capable of mimicking the behaviours observed *in vitro*. Here, a continuous multiphase model framework is proposed that has not been previously utilised to explore cell pattern formation within an engineered tissue environment. Crucially, the multiphase model framework can resolve both experimentally relevant boundary conditions and cell-level chemical and mechanical cues, in order to fully support the mechanisms associated with the migration of a cell phase within an engineered construct such as a hydrogel or scaffold. The multiphase model framework has been utilised in several studies of *in vitro* tissue culture and growth modelling [10], and was first adapted for this application by Lemon et al. [11,12]. A multiphase model approach has also been used to

---

study tumour growth [13–17]. More recently, Dyson et al. [18] extended the multiphase model framework to consider in more detail the mechanical effects of a fibrous collagen scaffold on cell migration and tissue growth. The multiphase model framework has additionally been demonstrated to capture chemotaxis-driven pattern formation, with cell aggregation demonstrated in 1D, and in a 2D thin film limit [19].

The behaviours and responses of endothelial cells, which can form vascular-like networks *in vitro*, have been investigated in a wide-range of *in vitro* assays [20–24]. Vascular endothelial growth factor (VEGF) is known to be essential for vascular network formation from knockout *in vivo* mouse studies that showed deletion of the gene responsible for VEGF production led to improper blood vessel formation and lethality [25,26]. The mechanisms by which VEGF may facilitate endothelial network formation are varied, including (i) influencing the direction of EC migration as a chemoattractant [27,28], (ii) accelerating the rate of EC migration by chemokinesis [29], (iii) affecting the rate of EC proliferation [30,31], and (iv) inducing/increasing EC production of matrix metalloproteinases (MMPs), enzymes responsible for degrading ECM proteins in the matrix surrounding the cell [30,32].

*In vitro* studies have found that HUVECs (human umbilical vein ECs) can form vascular networks alone without the addition of exogenous VEGF, particularly under low oxygen conditions [24,33,34]. Serini et al. [24] measured detectable levels of VEGF produced by both HUVECs (0.24 ng/ml) and microvascular ECs (0.67 ng/ml) after 3 h. Moreover, the role of VEGF gradients for EC network formation was confirmed by observing inhibition of network formation via the addition of either anti-VEGF, or via a saturating amount of exogenous VEGF [24]. Whilst the authors did not focus on the VEGF production of the HUVEC cells, Muangsanit et al. [34] observed the formation of tube-like structures after 4 days of culture in an aligned collagen construct, in the absence of exogenous VEGF or co-culture. However, the extent of network formation was significantly greater in co-culture with Schwann-like cells, which may be due to additional VEGF secretion of these cells [34].

To accurately model the dynamics of VEGF, the bioactivity of the scaffold material must also be considered. There is substantial evidence that some extracellular matrix proteins can bind soluble proteins, including growth factors [35]. In particular, it has been shown that fibronectin binds with VEGF [36], as does fibrinogen [37], fibrin [38], and heparin [39]. Using VEGF bound to a collagen–fibrinogen matrix, Chen et al. further demonstrated that matrix-bound VEGF elicited a stronger chemotactic response in endothelial cells than soluble VEGF [37]. Köhn-Luque et al. [40] demonstrated that exogenously added VEGF could bind to Matrigel pericellularly, and that this binding was co-localised with specific proteins including endothelial cell-secreted fibronectin and heparin. Using a hybrid computational model of chemotaxis-driven cell migration, the authors further suggested that the stronger response to bound VEGF could drive cell patterning [40].

Previous partial differential equation (PDE)-based vasculogenesis models have been predominantly based on a 2D assay in which endothelial cells are seeded on, as opposed to within, the extracellular matrix [8]. In these assays, the ECs have an initial 'free migration' period (∼ 9 hours [24,41]) in which they are detached from the matrix and do not have any mechanical interactions, whereas in a 3D environment there is no such initial period, and the cells are constrained by the surrounding hydrogel from conception. Notable models were able to replicate some of the resulting network properties, with similar qualitative behaviours as the initial cell density was varied [8,24,42]. In addition, the spatial scale of the *in vitro* network, determined by intervessel separation, was observed to be of the order of 200 μm and well matched by the numerical simulations [24]. However, interactions with the matrix including drag and traction were either not included [24], or included as a separate layer [42]. In comparison with 3D assays, the time-frame for patterning obtained in these models is much shorter [23,34], and often vascular-like patterning is observed transiently and would not persist to longer time-frames [42–45]. To date, there is an absence of a continuous model of vasculogenesis with a focus on mechanisms relevant to 3D *in vitro* culture, in which ECs are seeded within a scaffold or hydrogel.

In this paper, the impact of several commonly proposed mechanisms for vascular network formation are explored within the multiphase model framework; these are assessed using computational techniques including sensitivity analyses and parameter optimisation. Whilst simulation of the full 3D model will be of future value, we focus here on the 1D and 2D form of the model which are more amenable to the analysis required for model selection. We demonstrate long-term cell cluster formation, and a model form including VEGF–matrix binding is shown to form cell clusters on a comparable spatial scale to *in vitro* vascular network pattern size and structure. This is translated into 2D, where VEGF–matrix binding is also found to be required to match the spatial scale of vascular-like structures, and the impact of several possible additional mechanisms on the resulting network are considered. Future work may also consider the impact of total cell volume fraction, and an evolving ECM to support the connectivity and stability of patterning seen in more mature vascular networks.

In Section 2, an appropriate form of the multiphase model is presented, following an introduction of the model geometry and the assumptions made on the VEGF dynamics driving pattern formation. Two model forms are proposed: the 'core model', where VEGF is included as a solute only, and the 'binding model', in which two forms of VEGF, both matrix-bound and free, are included. The constitutive functional forms for intraphase cell forces and solute reaction terms are then motivated to complete the multiphase model. The more general binding model is then nondimensionalised for a 2D Cartesian geometry in Section 3 using parameter values motivated by literature, and boundary and initial conditions are imposed based on experimental conditions. A summary of the procedure for the computational implementation of the model in Python is then given in Section 4, with further details and verification of the numerical model available in Appendix A.2. The computational analyses methods used are outlined in Section 4.1. Results relating to the impact of the core model parameters and additional common mechanisms are presented in Sections 5.1–5.5. In particular, a steady state analysis of the core model is presented in Section 5.4. In Section 5.6, the impact of the addition of VEGF–matrix binding to the model is considered and shown to aid pattern formation on a spatial scale relevant to vascular network formation *in vitro*. The difference in spatial scale generated by the core and binding models in 1D and 2D is further demonstrated in Section 5.7, alongside additional network-related metrics for the 2D case.

## 2. Model outline

The multiphase model is based on the concept that the engineered tissue, commonly a cell-seeded hydrogel, is formed of three constituent phases: cells, water (culture media), and an extracellular matrix. Here, the hydrogel has been considered as being formed of a solid component (matrix phase), and a liquid component (water phase). Each of these phases is modelled based on their respective volume fraction at any given point in space $\mathbf{x}$ and at any given time $t$, the total of which always sums to unity. Thus, defining $n(\mathbf{x}, t)$ as the volume fraction of the cell phase, $w(\mathbf{x}, t)$ as the volume fraction of the water phase, and $m(\mathbf{x}, t)$ as the volume fraction of the matrix phase, a no-voids constraint $n + w + m = 1$ is imposed throughout our computational domain. For simplicity, we assume that the matrix phase is rigid and uniform, such that the volume fraction $m$ is a constant. The no-voids constraint in the hydrogel can thus be written as

$$n(\mathbf{x}, t) + w(\mathbf{x}, t) = \phi, \tag{1}$$

where $\phi = 1 - m$ is a constant representing the available volume fraction.

The general governing equations presented for the multiphase model below are derived following constitutive forms proposed by Lemon et al. [11] and subsequent model development papers [12,46,47]. Both
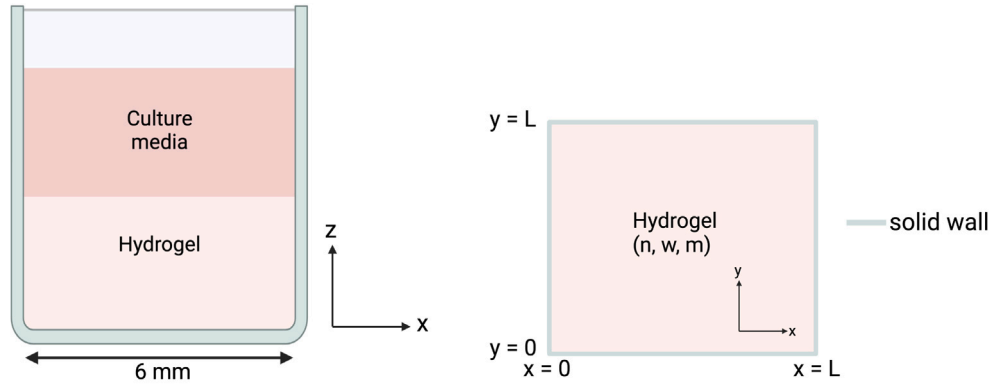
(a) Illustration of a well in a 96-well plate, commonly used for cellular hydrogel assays.

(b) Simplification of a simplified top-down view of a hydrogel in a well plate, using Cartesian coordinates.

**Fig. 1.** Illustration of the 2D Cartesian model geometry, based on a top-down slice of a hydrogel in a well plate.

cell and water phases are therefore modelled as continuous media, where the evolution of the spatial distributions of cell and water phases over time are governed by conservation laws of mass and momentum. We assume that cell proliferation is negligible, consistent with vascular network formation within a collagen hydrogel [33,48]. Hence, there is no transfer of volume between the three phases.

### 2.1. Model geometry and setup

The model geometry is based on a hydrogel in a well-plate, commonly utilised for experimental assays, illustrated in Fig. 1(a). In this setup, a cylindrical hydrogel, shown in light pink, is cultured under a layer of culture media, shown in dark pink. To focus firstly on the impact of cell mechanisms on the model outcomes, as opposed to the impact of experimental conditions, we take a simplified version of this geometry. Considering a top-down view, we model a 2D horizontal slice of the hydrogel using Cartesian coordinates. This 2D slice is illustrated in Fig. 1(b), where the boundaries of the domain are the solid walls of the well.

The scenario we wish to simulate is the evolution of the cell distribution over time, given an initial distribution of cells $n(\mathbf{x}, 0) = n_0(\mathbf{x})$, assuming cells located at a boundary wall cannot move (no-slip) and no-flux conditions also apply on the water phase at the boundary walls.

### 2.2. VEGF dynamics

The impact of the dynamics of the chemoattractant, VEGF, is investigated in this work. In what we refer to as the 'core' model for vascular network formation, VEGF is included as a solute, $c_u$, in the water phase, with possible dynamics including diffusion, production, uptake, and degradation. In the extended 'binding' model, VEGF is included in two forms: unbound VEGF, $c_u$, which is a solute in the water phase, and bound VEGF, $c_b$, which is bound to, but does not affect the volume fraction of, the extracellular matrix. This binding assumption is based on experimental evidence that endothelial cells produce small quantities of VEGF-binding matrix proteins, including fibronectin [40], which leads to pericellular VEGF–matrix binding.

The main driver of cell motion in the model is assumed to be the chemotactic response to the local VEGF concentration. Other key mechanisms affecting the spatial and temporal profile of cell and VEGF patterning include VEGF production and degradation, interphase drag forces, as well as cell diffusion. We also investigate the impact of additional commonly included mechanisms in models of vascular network formation and/or multiphase models of engineered tissues: VEGF uptake, cell–matrix traction, cell–cell aggregation, and cell–cell contact inhibition. In Section 5.6, we investigate the extended binding version of the model in which the chemotactic response of the cells to each form of VEGF is allowed to differ.

### 2.3. Model equations

As stated earlier, the general model equations, and constitutive terms selected here, are based on previous multiphase modelling works [12, 47], and the model assumptions outlined above.

The conservation of mass equation, governing the temporal and spatial distribution of the cell volume fraction, takes the form of an advection–diffusion equation

$$\frac{\partial n}{\partial t} + \nabla \cdot (n\mathbf{u_n}) = \nabla \cdot (D_n \nabla n), \tag{2}$$

where $D_n$ is the cell diffusion rate and $\mathbf{u_n}$ is the velocity of the cell phase. Although relatively small, cell diffusion is retained to aid numerical stability.

Due to the relatively short spatial scale (typically millimetres), in comparison to a long timescale for cell motility (typically hours — see Table 2), inertial effects are relatively small and hence neglected. The general conservation of momentum equations for the cell phase, governing the velocity field $\mathbf{u_n}$, are therefore represented by a balance between intraphase and external stresses resulting from the pressure between phases, so that

$$\nabla \cdot (n\boldsymbol{\sigma}_n) + \mathbf{f}_{nw} + \mathbf{f}_{nm} = 0, \tag{3}$$

where $\sigma_n$ is the stress tensor for the cell phase, and $\mathbf{f}_{ij}$ represents the interphase force of phase $j$ on phase $i$ noting that, by Newton's third law, $\mathbf{f}_{ij} = -\mathbf{f}_{ji}$. The cell phase is assumed to behave as a Newtonian fluid, thus

$$\sigma_n = -p_n \mathbf{I} + \tau_n$$
$$= -\left(p_n + \frac{2}{3}\mu_n (\nabla \cdot \mathbf{u_n})\right)\mathbf{I} + \mu_n \left(\nabla \mathbf{u_n} + \nabla \mathbf{u_n}^T\right)$$

where $p_n$ is the cell intraphase pressure, $\tau_n$ is the deviatoric part of the stress tensor, and $\mu_n$ is the cell intraphase shear viscosity. Constitutive forms of the intraphase and interphase forces are prescribed in the following sections following Lemon et al. [11].

#### 2.3.1. Cell intraphase pressure

The cell intraphase pressure, $p_n$, is split into multiple parts: a water pressure component, $p_w$; the contribution of potential cell–cell interactions, denoted $\Pi_n$; the contribution of chemotaxis, denoted $\Pi_c$; and a final term to account for cell-matrix interactions, such that

$$p_n = p_w + \Pi_n + \Pi_c + m\psi_{nm},$$

where $\psi_{nm}$ is the traction force between the cells and the matrix phase. This constitutive form, commonly adopted in multiphase models [12, 46,47], is based on the concept that the cell phase will experience the same 'inactive' pressure as the water phase, given that cells are mostly

formed of water, with additional 'active' pressures due to interactions with other cells, chemical solutes, and the extracellular matrix.

The cell–cell interaction pressures, $\Pi_n$, can include: (i) cell–cell contact inhibition, e.g. $\Pi_i = \delta_n n^2/(\phi - n)$ [46]; and (ii) cell–cell aggregation, e.g. $\Pi_a = -\nu n$. There are several possible forms for the chemotaxis term, $\Pi_c$, including $\Pi_c = \chi \exp\left(-\frac{c}{c_M}\right)$ [47]. We consider chemotaxis to act as a dominant cell intraphase pressure and include it as a key mechanism; the possible influence of contact inhibition and cell–cell aggregation is explored subsequently in Section 5.5. The form of chemotaxis here is selected such that the chemotactic response is higher in gradients of low VEGF concentration, such as in regions of low cell volume fraction [47]. Investigating the impact of the choice of the chemotaxis functional form is left to future work.

The cell-matrix traction force, characterised by the parameter $\psi_{nm}$, is taken to be a negative constant to represent the cells' affinity to the ECM. Hence, we write $\psi_{nm} = -\eta$, where $\eta$ is a positive constant.

### 2.3.2. Interphase forces

The interphase forces are split into two components: an interphase pressure, $p_{ij}$, and a drag term, $\gamma_{ij}$ [11]. The general force exerted by phase $j$ on phase $i$ is given by

$$\mathbf{f}_{ij} = p_{ij}j\nabla i - p_{ji}i\nabla j + \gamma_{ij}ij\left(\mathbf{u}_j - \mathbf{u}_i\right). \tag{4}$$

The interphase pressures $p_{ij}$ are similarly decomposed into a 'contact-independent' pressure equal to the water pressure, $p_w$, and additional 'active' pressures. The only 'active' pressure between phases considered here is the traction-induced pressure force between the cells and extracellular matrix introduced previously, $\psi_{nm} = -\eta$. Each interphase force term can hence be written as

$$\mathbf{f}_{nw} = p_w w\nabla n - p_w n\nabla w$$

$$\mathbf{f}_{nm} = (p_w - \eta)m\nabla n - \gamma_{nm}nm\mathbf{u_n},$$

where drag between the cell and water phase has been neglected, motivated by its relative magnitude as discussed in [12], and the desire to keep the conservation of momentum equations uncoupled.

Substituting these terms into (3) and applying the no-voids constraint, the conservation of momentum equation for the cell phase becomes

$$-n\nabla p_w - \nabla\left(n\Pi_n + n\Pi_c\right) + \nabla\left(n\mu_n\boldsymbol{\tau_n}\right) - \gamma_{nm}nm\mathbf{u_n} - \eta m\nabla n = 0, \tag{5}$$

### 2.3.3. Water phase

A similar process to that of the cell phase can be applied to the water phase. Defining $\mathbf{u_w}$ as the velocity of the water phase, conservation of total volume fraction implies

$$\frac{\partial w}{\partial t} + \nabla \cdot \left(w\mathbf{u_w}\right) = 0, \tag{6}$$

Inertia is once again neglected and the drag induced by the matrix phase is assumed to be the dominant interaction on motion of the water phase. Conservation of momentum for the water-phase thus yields

$$-w\nabla p_w - \gamma_{wm}wm\mathbf{u_w} = 0. \tag{7}$$

which is characteristic of Darcy's law [12], where the drag parameter $\gamma_{wm}$ acts as an effective viscosity of the water phase within the porous matrix phase, with an *effective permeability* of $m^{-1}$.

### 2.3.4. VEGF concentration

Unbound VEGF, $c_u$, is modelled as a solute in the water phase, for which the general conservation of mass equation takes the form of the following advection–diffusion–reaction equation,

$$\frac{\partial(c_u w)}{\partial t} + \nabla \cdot \left(c_u w\mathbf{u_w}\right) = \nabla \cdot \left(D_u w\nabla c_u\right) + R_u, \tag{8}$$

where $D_u$ is the diffusion coefficient for unbound VEGF, and $R_u$ is a reaction term that is defined in subsequent Sections 2.3.5 and 2.3.6 for the core and binding model respectively.

Bound VEGF, $c_b$, included in the binding model, is assumed to be bound to the matrix phase, but has a negligible associated volume such that the matrix volume fraction remains constant. Hence, the conservation of mass equation for bound VEGF takes the following form,

$$\frac{\partial(c_b m)}{\partial t} = R_b, \tag{9}$$

where $R_b$ is a reaction term defined below in Section 2.3.6.

### 2.3.5. Core model

Excluding VEGF–matrix binding, the possible VEGF dynamics include diffusion, production and uptake by endothelial cells, and cell-independent degradation. The reaction term for the VEGF solute in the core model, based on (8), is thus written as

$$R(n, w, c) = \alpha(n, w, c)n - \kappa(n, w, c) - \delta c,$$

where $\alpha(n, w, c)$ is a production function, $\kappa(n, w, c)$ is an uptake function, and $\delta$ is a constant degradation rate. Although uptake of VEGF (which spans the ligand-receptor binding and internalisation process of VEGF into the cell) is required for a cell response, in our model we decouple the two stages of the biological process and take uptake to represent the removal of VEGF from the solvent only.

A Michaelis–Menten function of the form $\kappa(n, w, c) = \kappa nwc/(c + K)$ has previously been used to describe cellular uptake of VEGF in an angiogenesis model [49], where $\kappa$ is the maximal uptake rate, and $K$ is the concentration of VEGF at which uptake is half-maximal. A Michaelis–Menten term has also been used to model production, for example for fibronectin production by endothelial cells during angiogenesis [49]. As the local concentration of fibronectin increases, the rate of production slows, until it reaches a maximum rate. Alternatively, in a fluids-based mechano-chemical model of vasculogenesis, Tosin et al. [42] consider a production rate $\alpha(n)$ with non-linear dependence on the cell density. The authors assumed a production rate that reached a finite maximum for $n = 0$ and monotonically decreased for $n > 0$, reaching a negligible level once the local cell density represented a sizeable cluster. Following Tosin et al. [42], we select the functional form $\alpha(n) = \alpha(\phi - n)$ that exhibits the same behaviour when modelling a cell volume fraction as opposed to cell density. Including these reaction terms, the governing equation for VEGF in the core model is therefore assumed to take the form

$$\frac{\partial(cw)}{\partial t} + \nabla \cdot \left(cw\mathbf{u_w}\right) = \nabla \cdot \left(D_u w\nabla c\right) + \alpha n(\phi - n) - \frac{\kappa nwc}{c + K} - \delta c. \tag{10}$$

### 2.3.6. Binding model

To consider the simplest model of VEGF binding in the first instance, any diffusion, uptake, or direct production of bound VEGF $c_b$ is neglected. There is some evidence that binding to the extracellular matrix reduces the rate of degradation of proteins including VEGF [37,40]; however, this difference is neglected for now such that the rate of degradation of bound and unbound VEGF is considered equal and represented by the same parameter $\delta$. The experimental analysis of Köhn-Luque et al. [40] is suggestive of VEGF-binding to specific local cell-deposited ECM proteins such as fibronectin. A more complex model may consider secretion of fibronectin and VEGF-fibronectin binding, but to simplify the mechanism here, the pericellular location of the VEGF binding sites can be accounted for by choosing the binding rate to be proportional to the local cell density.

The addition of a VEGF–matrix binding mechanism introduces three new parameters: the binding rate, $k_b$, the unbinding rate, $k_u$, and the strength of the chemotactic response to bound VEGF, $\chi_b$. For clarity, the strength of the chemotactic response to free (unbound) VEGF is denoted $\chi_u$ in both the core and binding model.

Including binding with the matrix, the reaction term for unbound VEGF, $R_u$, can be written as

$$R_u(n, w, m, c_u, c_b) = \alpha n(\phi - n) - \frac{\kappa nwc_u}{K + c_u} - \delta c_u - k_b mn(c_u w) + k_u w(c_b m)$$

**Table 1**
Variable and parameter definitions for the general and specified multiphase model.

| Variable/parameter | Definition |
|---|---|
| n | Cell volume fraction |
| w | Water volume fraction |
| m | Matrix volume fraction |
| $\phi = 1 - m$ | Available volume fraction |
| $c_i$ $(i = \text{u, b})$ | Unbound/bound VEGF concentration |
| $\mathbf{u_i} = (u_i, v_i)$ $(i = \text{n, w})$ | Cell/water velocity |
| $D_i$ $(i = \text{n, u})$ | Diffusion rate of cells/unbound VEGF |
| $R_i$ $(i = \text{u, b})$ | Reaction term for unbound/bound VEGF |
| $\sigma_i$ $(i = \text{n, w})$ | Cell/water stress tensor |
| $f_{ij}$ $(i, j = \text{n, w, m}, i \neq j)$ | Interphase force exerted on phase $i$ by phase $j$ |
| $p_i$ $(i = \text{n, w})$ | Pressure in cell/water phase |
| $\mu_n$ | Cell viscosity |
| $\boldsymbol{\tau_n}$ | Cell deviatoric stress tensor |
| $p_{ij}$ $(i, j = \text{n, w, m}, i \neq j)$ | Interphase pressure exerted on phase $i$ by phase $j$ |
| $\gamma_{ij}$ $(i, j = \text{n, w, m}, i \neq j)$ | Drag coefficient between phase $i$ and phase $j$ |
| $\psi_{nm}$ | Traction coefficient between cell and matrix phases |
| $\eta$ | (constant) traction pressure between cell and matrix phases |
| $\delta_n$ | cell-cell contact inhibition pressure |
| $\nu$ | cell-cell aggregation pressure |
| $\chi_i$ $(i = \text{u, b})$ | Chemotactic response to unbound/bound VEGF |
| $\alpha$ | VEGF production rate |
| $\kappa$ | VEGF uptake rate |
| $K$ | VEGF concentration at which uptake is half-maximal |
| $\delta$ | VEGF degradation rate |
| $k_i (i = u, b)$ | VEGF-matrix unbinding/binding rate |

where $k_b$ and $k_u$ are the binding and unbinding rates respectively, and the dependence of binding on $n$ represents the indirect coupling of the local cell volume fraction with the local availability of binding sites via fibronectin production. The dependence on $w$ and $m$ in the binding terms is due to the transfer of the VEGF from within the water phase to within the matrix phase, and vice versa. On the other hand, the reaction term for bound VEGF, $R_b$, takes the form

$$R_b(n, w, m, c_u, c_b) = k_b mn(c_u w) - k_u w(c_b m) - \delta c_b.$$

Hence, the full governing equations for unbound and bound VEGF are

$$\frac{\partial(c_u w)}{\partial t} + \nabla \cdot (c_u w \mathbf{u_w}) = \nabla \cdot (D_u w \nabla c_u) + \alpha n(\phi - n) - \frac{\kappa n w c_u}{c_u + K} \tag{11}$$
$$- k_b mn(c_u w) + k_u w(c_b m) - \delta c_u,$$

and

$$\frac{\partial(c_b w)}{\partial t} = k_b mn(c_u w) - k_u w(c_b m) - \delta c_b, \tag{12}$$

respectively.

### 2.3.7. Summary

The governing equations are now ((1), (2), (5)–(7), (10)) for the core model and ((1), (2), (5)–(7), (11), (12)) for the binding model. The variable and parameter definitions for the general and specified models are given in Table 1. Given that the core model is a reduction of the binding model, obtained when $k_u = k_b = 0$, $\chi_b = 0$, and $c_b = 0$, nondimensionalisation and numerical verification are presented for the binding version of the model only.

## 3. Dimensional analysis

### 3.1. Dimensional parameter values

The typical lengthscale is chosen to be based on the dimensions of a 96-well plate, shown in Fig. 1(a). Given a diameter of around 6 mm, and variable hydrogel height of 1–5 mm, we set the representative lengthscale $L$ to be within this range at 3 mm. The representative timescale is chosen to be related to the time under which network formation is observed *in vitro*, shown to span from a few hours [24], to 24–48 h [49], to several days [50], dependent on the geometry and experimental conditions. A typical timescale of $T = 10^5$ s, $\sim 27$ h, is

chosen to match the order of the timescale of chemotaxis-driven pattern formation, which is the focus of the model presented here.

Table 2 outlines the estimated timescales for the main processes considered by the model. Excluding cell diffusion, each process considered is significant on the chosen length scale given a timescale of interest of 24–96 h. Despite the significantly longer timescale and consequently large Péclet number, cell diffusion is maintained in the computational model to improve numerical stability. The remaining cell- and solute-related parameters required for the model are discussed below.

### 3.1.1. Cell-related parameters

Using Stokes flow, Lemon and King [12] estimated the magnitude of the water-matrix drag and cell-matrix drag term, where the latter was found to be several orders of magnitude larger. The estimate of cell viscosity, $\mu_n = 1 \times 10^4$ N m$^{-2}$ s, is based on experimental evidence further reported by Lemon and King [12].

The strength of chemotaxis, $\chi_i$ $(i = u, b)$, is modelled as a stress within this framework and is not amenable to experimental derivation. A key aim of this paper is to first ascertain possible dimensionless values of $\chi_u$ such that chemotactic effects are dominant in the core model. The cell-matrix traction constant $\eta$ is explored in a similar fashion, as is $\chi_b$ in the subsequent binding model.

### 3.1.2. VEGF-related parameters

There is scant quantitative data regarding the concentration of VEGF produced by endothelial cells. Serini et al. [24] measured detectable levels of VEGF after 3 h in the range 0.24 ng/ml – 0.67 ng/ml; similarly Nomura et al. [58] quoted that HUVECs produced a concentration of 0.15 ng/ml at 10% oxygen. Based on these estimates, the concentration of 1 ng/ml is taken as the scaling for VEGF concentration, $c_M$.

Parameters including VEGF production and uptake rates are highly dependent on cell type, and again scant quantitative data is available. VEGF production rates used in previous models in literature are often quoted as per area per second, reflecting the 2D *in vitro* setup of the assay being modelled. A crude conversion made from estimates from other cell types, including from cells in the endoderm [56], and from ADSCs in 3D culture [59], suggests a broad dimensional range of $\alpha$ from $1 \times 10^{-13}$ to $1 \times 10^{-11}$ g ml$^{-1}$ s$^{-1}$. However, parameter analysis methods are required here to determine a suitable range of values that may

**Table 2**

Estimated timescales of relevant dynamic processes. Estimates are based on the hydrogel length scale L = 3 mm, and a typical concentration of VEGF, 1 ng/ml. References are given for each estimate where applicable.

| Process | Estimated timescale | Reference(s) |
|---|---|---|
| Cell diffusion | $2.5 \times 10^3 - 2.5 \times 10^4$ h | [51–53] |
| VEGF diffusion in a hydrogel | 250 h | [24,40,54] |
| VEGF diffusion in media | 25 h | [55] |
| VEGF production | 0.05 h | [24] |
| VEGF half-life | 0.1 h – 3 h | [24,37,40,56,57] |
| Vascular network formation | 9 h – 4 d | [24,33,49] |
| Cell directed migration in a hydrogel | 80 h | [27,51] |

lead to qualitatively different model outcomes, including the parameter sweep presented in Section 5.1.

Köhn-Luque et al. [40] fit experimental data to a similar ODE model of binding and unbinding of VEGF, based on an experimental assay that observed the pericellular binding of exogenously added VEGF in Matrigel. The ODE governing bound VEGF was in this case given by

$$\frac{\partial (b)}{\partial t} = k_{on}^* U_{eq} - k_{off} b, \tag{13}$$

where $b$ is the concentration of bound VEGF, $U_{eq}$ is the equilibrium concentration of unbound VEGF, $k_{on}^*$ is the rate of binding, taking into account the equilibrium concentration of binding sites, and $k_{off}$ is the rate of unbinding. Comparing this with Eq. (12), and using the values of $k_{on}^*$ and $k_{off}$ determined by Köhn-Luque et al. [40], the values derived for $k_b$ and $k_u$ are $k_b \approx 0.05 \pm 0.01 \text{ s}^{-1}$ and $k_u \approx 3.7 \times 10^{-3} \pm 3.97 \times 10^{-4} \text{ s}^{-1}$. The impact of the experimental uncertainty will be considered via a sensitivity analysis in Section 5.6.

### 3.2. Nondimensionalisation

A 2D Cartesian model is considered to approximate a top-down view of the geometry, considered to be square for simplicity, as shown in Fig. 1(b). The following dimensionless variables are used for nondimensionalisation of the 2D Cartesian model, with nondimensionalised versions denoted by an asterisk (*):

$$x^* = \frac{x}{L}, \qquad y^* = \frac{y}{L}, \qquad t^* = \frac{t}{T}, \qquad c_{u,b}^* = \frac{c_{u,b}}{c_M},$$

$$D_{n,u}^* = \frac{D_{n,u}T}{L^2}, \quad u_{n,w}^* = \frac{u_{n,w}T}{L}, \quad v_{n,w}^* = \frac{v_{n,w}T}{L}, \qquad \gamma_{nm}^* = \frac{\gamma_{nm}L^2}{\mu_n},$$

$$\chi_{u,b}^* = \frac{\chi_{u,b}T}{\mu_n}, \qquad \eta^* = \frac{\eta T}{\mu_n}, \qquad p_w^* = (p_w - p_{atm})\frac{T}{\mu_n}, \qquad \alpha^* = \frac{\alpha T}{c_M},$$

$$\kappa^* = \frac{\kappa T}{c_M}, \qquad K^* = \frac{K}{c_M}, \qquad k_{u,b}^* = k_{u,b}T, \qquad \delta^* = \delta T.$$

After nondimensionalisation, dropping asterisks, the 2D Cartesian model comprises nine coupled PDEs. The following dimensionless equations govern cell volume fraction, $n$, water volume fraction, $w$, water velocity components, $u_w$ and $v_w$, water pressure, $p_w$, unbound and bound VEGF concentrations, $c_u$ and $c_b$, and cell velocity components, $u_n$ and $v_n$:

$$\frac{\partial n}{\partial t} + \frac{\partial}{\partial x}\left(nu_n\right) + \frac{\partial}{\partial y}\left(nv_n\right) = D_n\left(\frac{\partial^2 n}{\partial x^2} + \frac{\partial^2 n}{\partial y^2}\right), \tag{14}$$

$$n + w = \phi, \tag{15}$$

$$\frac{\partial w}{\partial t} + \frac{\partial}{\partial x}\left(wu_w\right) + \frac{\partial}{\partial y}\left(wv_w\right) = 0, \tag{16}$$

$$u_w = -\frac{1}{\gamma_{wm}m}\frac{\partial p_w}{\partial x}, \tag{17}$$

$$v_w = -\frac{1}{\gamma_{wm}m}\frac{\partial p_w}{\partial y}, \tag{18}$$

$$\frac{\partial (c_u w)}{\partial t} + \frac{\partial (c_u w u_w)}{\partial x} + \frac{\partial (c_u w v_w)}{\partial y} = \frac{\partial}{\partial x}\left(D_u w \frac{\partial c_u}{\partial x}\right) + \frac{\partial}{\partial y}\left(D_u w \frac{\partial c_u}{\partial y}\right)$$

$$+\alpha n(\phi - n) - \frac{\kappa n w c_u}{c_u + K} - k_b mn(c_u w) + k_u w(c_b m) - \delta c_u, \tag{19}$$

$$\frac{\partial (c_b w)}{\partial t} = k_b mn(c_u w) - k_u w(c_b m) - \delta c_b, \tag{20}$$

$$-n\frac{\partial p_w}{\partial x} - \frac{\partial}{\partial x}\left(n\chi_u \exp(-c_u) + n\chi_b \exp(-c_b)\right) - \frac{\partial}{\partial x}\left(vn^2 + \frac{\delta_n n^3}{\phi - n}\right)$$

$$+\frac{2}{3}\frac{\partial}{\partial x}\left[n\left(2\frac{\partial u_n}{\partial x} - \frac{\partial v_n}{\partial y}\right)\right] + \frac{\partial}{\partial y}\left[n\left(\frac{\partial u_n}{\partial y} + \frac{\partial v_n}{\partial x}\right)\right]$$

$$-\gamma_{nm}nmu_n - \eta m\frac{\partial n}{\partial x} = 0, \tag{21}$$

$$-n\frac{\partial p_w}{\partial y} - \frac{\partial}{\partial y}\left(n\chi_u \exp(-c_u) + n\chi_b \exp(-c_b)\right) - \frac{\partial}{\partial y}\left(vn^2 + \frac{\delta_n n^3}{\phi - n}\right)$$

$$+\frac{\partial}{\partial x}\left[n\left(\frac{\partial u_n}{\partial y} + \frac{\partial v_n}{\partial x}\right)\right] + \frac{2}{3}\frac{\partial}{\partial y}\left[n\left(2\frac{\partial v_n}{\partial y} - \frac{\partial u_n}{\partial x}\right)\right]$$

$$-\gamma_{nm}nmv_n - \eta m\frac{\partial n}{\partial y} = 0. \tag{22}$$

All possible additional mechanisms are shown including contact inhibition, $\delta_n$, cell–matrix traction, $\eta$, VEGF uptake, $\kappa$, and cell–cell aggregation, $v$. The estimates for the values of the dimensionless parameters in the model are given in Table 3 where possible.

In order to solve the model, the water conservation of momentum Eq. (17), (18) were substituted into the water conservation of mass Eq. (16) to obtain a Poisson equation for water pressure, $p_w$,

$$\frac{\partial w}{\partial t} - \frac{1}{\gamma_{wm}m}\frac{\partial}{\partial x}\left(w\frac{\partial p_w}{\partial x}\right) - \frac{1}{\gamma_{wm}m}\frac{\partial}{\partial y}\left(w\frac{\partial p_w}{\partial y}\right) = 0, \tag{23}$$

which is used in place of Eq. (16).

### 3.3. Boundary conditions

Based on Fig. 1(b), no-flux conditions are applied on all boundaries for the cell phase, water phase (including water pressure), and the unbound VEGF concentration. No-slip conditions are also applied to the cell phase on the boundaries. Thus we have the boundary conditions

$$u_n = 0, \quad v_n = 0, \quad \frac{\partial n}{\partial x} = 0, \quad \frac{\partial c_u}{\partial x} = 0, \quad \frac{\partial p_w}{\partial x} = 0, \quad \text{at } x = 0, 1, \text{ and}$$

$$u_n = 0, \quad v_n = 0, \quad \frac{\partial n}{\partial y} = 0, \quad \frac{\partial c_u}{\partial y} = 0, \quad \frac{\partial p_w}{\partial y} = 0, \quad \text{at } y = 0, 1.$$

Equivalent no-flux and no-slip boundary conditions are adopted when considering a reduced 1D version of the model, which is used for benchmarking and as described in Section 4.1 for efficient parameterisation in order to exploit computationally expensive analysis methods.

### 3.4. Initial conditions

The hydrogel is assumed to contain an initial cell distribution at rest, with no bound or unbound VEGF present, given that the culture media used for the hydrogel preparation does not contain VEGF. Thus we have the initial conditions

$$n(x, y, 0) = n^0(x, y), \quad u_n(x, y, 0) = 0, \quad v_n(x, y, 0) = 0,$$

$$p_w(x, y, 0) = 0, \quad c_{u,b}(x, y, 0) = 0, \quad \text{and} \quad w(x, y, 0) = \phi - n^0(x, y). \tag{24}$$

**Table 3**

Dimensionless parameter values where estimates can be made. The dimensionless values are obtained by nondimensionalisation of the model parameters as written in Section 3.2.

| Parameter | Definition | Dimensionless value |
|---|---|---|
| m | Matrix volume fraction | 0.03 |
| $\phi$ | Available volume fraction | 0.97 |
| $D_n$ | Cell diffusion rate | $1 \times 10^{-4}$ |
| $D_u$ | Unbound VEGF diffusion rate in hydrogel | 0.1 |
| $\gamma_{wm}$ | Water-matrix drag | $1.6 \times 10^{-2}$ |
| $\gamma_{nm}$ | cell-matrix drag | $\gamma_{wm} < \gamma_{nm} \leq 10^5$ |
| $\alpha$ | VEGF production rate | $100 - 1 \times 10^4$ |
| $\kappa$ | VEGF uptake rate | $0 \leq \kappa \leq \alpha$ |
| K | VEGF concentration at which uptake is half-maximal | $0 - 1$ |
| $k_b$ | VEGF-matrix binding rate | $5 \times 10^3$ |
| $k_u$ | VEGF-matrix unbinding rate | 370 |
| $\delta$ | VEGF degradation rate | $0.3 - 400$ |
| $\chi_{u,b}$ | chemotactic response to unbound or bound VEGF | $0 - 500$ |
| $\eta$ | cell-matrix traction strength | $0 - 100$ |
| $\nu$ | cell-cell aggregation strength | $0 - 100$ |
| $\delta_n$ | cell-cell contact inhibition | $0 - 100$ |

The way in which a random initial cell distribution, constituting 5% of the total hydrogel volume, was implemented numerically is described in Section 4.2.

## 4. Numerical methods

The 1D and 2D Cartesian model equations were solved numerically in Python by discretising the model equations using the finite-difference method. The algorithmic approach taken to solve the coupled equations within each timestep is outlined in Appendix A.1. The numerical model was verified by using 1D analytical solutions, verifying the grid and time convergence, and monitoring conservation of the cell volume fraction. These convergence plots for the 2D numerical model are presented in Appendix A.2. The full code to solve the 1D and 2D core and binding models and generate the results figures is openly available on GitHub.

Here, the main computational techniques used to analyse the model, sensitivity analysis and parameter optimisation, are introduced. Additionally, Section 4.1.1 outlines how the 1D and 2D metrics were quantified. Section 4.2 outlines how the initial condition was set.

### 4.1. Computational analysis methods

To assess the capabilities of the core model to simulate cell patterning, the computational analyses focused on (i) identifying qualitatively distinct cell distribution outcomes, and (ii) assessing the timing and stability of pattern formation. The overall aim of the analyses was to identify a suitable model that was capable of qualitatively matching *in vitro* data, including the temporal and spatial scale of pattern formation. Additionally, the analyses sought to minimise the number of parameters required in the model to meet these conditions. To exploit computational techniques whilst minimising computational expense, initial analyses were conducted on the 1D version of Eqs. (14)–(22), assuming no *y*-dependence. Such model reduction is justified as the 1D model retains the likely mechanisms of cluster formation. Indeed, the conclusions of these 1D analyses are shown to translate well to the 2D model throughout Section 5.

### 4.1.1. Output metrics

In the 1D model, patterning arises in the form of cell clusters. Here, the number of cell clusters formed within the domain is considered to be the main outcome metric of interest. Additionally, cluster spacing and cluster width are related to characteristic pattern size in 2D, and can be observed *in vitro* and qualitatively matched [42]. Hence, though not independent from the number of clusters, these are useful secondary metrics that can be used to assess biological plausibility of the model. In the following analyses, the number of cell clusters was

calculated by applying a low threshold to the cell volume fraction distribution, and then identifying the number of discrete objects.

In 2D, patterning arises as vascular-like structures that may form a network. In this case, the spacing between clusters or the diameter of 'voids' created by connected mesh-like patterning can be used to assess the spatial scale of patterning. To determine vessel width and spacing, several 1D slices of the 2D simulation output in each dimension are taken and treated in the same manner to the 1D model, using methods in `scipy.signal` to identify peaks and determine vessel widths. These metrics are utilised to compare the characteristic spatial scale of each model in Section 5.7. Additional suitable metrics here include the average number of branches per node, average branch length, the number and diameter of network loops (lacunae), and the connectivity of the network. Presented in Section 5.7, these metrics were quantified by skeletonising the image using `skimage.morphology.skeletonize` after taking a low threshold, constructing a network from the skeleton using `sknw`, and importing into `networkx` for network analysis. For the loop (lacunae) diameters, the loops were identified in networkx and their coordinates exported to an array for minor axis length measurement using `skimage.measure.regionprops`.

### 4.1.2. Sensitivity analysis

A sensitivity analysis can determine both the model tolerance to variation in parameters, *i.e.* robustness, and the parameters which have the most influence over a particular model outcome. Sensitivity analysis can play an important role in model selection by identifying parameters that have negligible impact on model outcomes, and hence are superfluous. It is beneficial to reduce the number of key parameters as more complex models require significantly more data than may be plausible, as well as to avoid over-fitting of the model. Additionally, this technique can be used to determine which changes in experimental variables have the most significant impact on vascular network formation in the model.

In Python, an open source library `SALib` provides a sensitivity analysis framework for any user-developed function [60]. `SALib` runs two functions: parameter space sampling (`SALib.sample`), and an analysis of the variation of model outputs with respect to the sampled parameter inputs (`SALib.analyze`). Here, the Sobol method was selected to provide the most detailed information for total, first-order, and second-order parameter interactions [61]. The resulting Sensitivity indices (Si) are a measure, between 0 and 1, of a parameter's influence on the outcome metric. Very small values, comparative to the magnitude of the confidence level of the index, can be assumed to be negligible.

**Table 4**

Dimensionless parameter bounds for the core model parameters used for computational model analysis.

| Core parameter | Minimum value | Maximum value |
|---|---|---|
| $\chi_u$ | 100 | 500 |
| $\gamma_{nm}$ | 0.1 | 10 |
| $\alpha$ | $1 \times 10^3$ | $1 \times 10^4$ |
| $\delta$ | 10 | 100 |

**Table 5**

Total Sensitivity index for each of the core parameters, based on number of cell clusters formed, at $t = 1, 2, 3$, and 4 respectively. The parameter bounds used are given in Table 4.

| $t$ [-] | 1 | 2 | 3 | 4 |
|---|---|---|---|---|
| VEGF degradation rate | 0.67 | 0.76 | 0.81 | 0.84 |
| VEGF production rate | 0.55 | 0.58 | 0.59 | 0.58 |
| Chemotaxis strength | 0.40 | 0.35 | 0.31 | 0.29 |
| Cell-matrix drag | 0.34 | 0.25 | 0.23 | 0.2 |

**Table 6**

Dimensionless parameter values found to maximise the number of cell clusters formed at $t = 2$ and $t = 4$ respectively, using the particle swarm optimisation method.

| $t$ [-] | 2 | 4 |
|---|---|---|
| average no. of clusters | 5.0 | 5.4 |
| VEGF degradation rate | 99.6 | 90.0 |
| VEGF production rate | $7.41 \times 10^3$ | $8.92 \times 10^3$ |
| Chemotaxis strength | 367 | 401 |
| Cell-matrix drag | 4.16 | 3.91 |

### 4.1.3. Particle swarm optimisation

Parameter optimisation is an umbrella term for computational methods that seek to find an input parameter value, or set of input values, that produce an optimal model outcome as determined by a user-defined metric. Here, a particle swarm optimisation (PSO) algorithm has been selected which, given a metric to minimise, can find the optimal global or local point of the parameter set through an iterative procedure. In Python, the open source module PySwarms offers an implementation of this algorithm for any user-defined function and metric [62].

### 4.2. Initial cell distribution

A random initial cell distribution was generated using the numpy function random.normal, which takes an input of the mean value, standard deviation, and size of the grid. This function uses a random number generator, the seed of which can be fixed using random.seed(), to generate a sequence or array of random numbers taken from a normal distribution as specified by the function inputs. To control the spatial scale of the variability in the initial cell distribution, this function was used alongside numpy.repeat to set the spatial variability to be on the same scale as the width of a single cell or cluster of cells.

A sensitivity analysis was conducted which indicated that the relative standard deviation nor spatial variability of the initial condition have a significant impact on the simulation outcome (results not shown). However, the random seed used to generate the initial cell distribution did have a significant effect on the simulation results. Hence, it is appropriate to treat the model stochastically, running analyses on model statistics over many random initial conditions, as opposed to individual outcomes.

## 5. Results and discussion

### 5.1. Effect of core model parameters on cell cluster formation

We consider four parameters of the 'core' model as identified by literature review to be most essential for the model: $\alpha$, the VEGF production rate; $\delta$, the VEGF degradation rate; $\chi_u$, the chemotaxis strength; and $\gamma_{nm}$, the cell-matrix drag. To verify that the parameter bounds informed by intuition and literature review are suitable for a sensitivity analysis, a manual parameter sweep was first conducted on a subset of parameter samples to gain some preliminary information about the regions of the parameter space that may lead to qualitatively distinct cell distribution outcomes. The dimensionless parameter bounds used for the following analyses are given in Table 4.

To conduct the parameter sweep, 768 parameter samples were generated using a Saltelli sampler (compared to 6144 for the full sensitivity analysis), and the model was run for each sample until $t = 2$ ($\sim 54$ h), recording the number of clusters observed. The profile of a subset of this data, for samples in which two or more clusters were observed at $t = 2$, is presented in Fig. 2. The histograms presented as marginal plots illustrate the values of each parameter present in this subset, where a clear skew towards high or low values of each parameter can be identified for each of the core parameters. The scatter plots are used to illustrate potential relationships between two parameter values, with

a regression line plotted for each. The two parameter relationships presented here were chosen based on their correlation coefficients, and represent a positive relationship between VEGF production rate and degradation ($r = 0.64$), and between chemotaxis strength and cell-matrix drag ($r = 0.29$) respectively.

In Fig. 3, the parameter samples are labelled based on the specific number of clusters produced. Fig. 3(a) illustrates the values of VEGF production rate and VEGF degradation rate for which either 2–3, 3–4, or more than 4 clusters were produced. Likewise, Fig. 3(b) illustrates the values of chemotaxis strength and cell-matrix drag which produce different numbers of clusters. Both plots suggest reasonably clear focus regions in the parameter space that yield a large number of clusters from model simulations.

A sensitivity analysis was also conducted on these four core parameters, using the number of clusters formed as the output metric. The analysis was based on the average simulation output over 10 random initial conditions. The same 10 random seeds are used in the computational analysis throughout this paper. Table 5 presents the total Sensitivity index for each parameter at $t = 1, 2, 3$ and 4 respectively. The decrease in Si over time for chemotaxis strength and cell-matrix drag suggests that these parameters play a role in the timing of cluster formation, but are less influential over the number of clusters formed long-term. The most influential parameters on cell clustering are hence related to VEGF production and degradation, as their Si values increase and/or remain high.

### 5.2. Spatial scale of core model cell cluster formation

In the parameter sweep presented above, the maximum number of clusters obtained for the parameter range used was 4.7, suggesting that it is uncommon for 5 or more clusters to be produced in this domain by the core four-parameter model within the parameter bounds given. Given that this domain has equivalent dimensional length $L = 3$ mm, a much higher number of clusters would be expected if this model were to represent the scale of capillaries. To verify the maximum number of clusters the core model is able to produce, and for which parameter values, a particle swarm optimisation (PSO) algorithm was utilised to maximise the average number of clusters produced within the parameter bounds of Table 4.

The optimal parameter values found by PSO to maximise the average number of clusters at $t = 2$ and $t = 4$ are presented in Table 6. These indicate that generally 5–6 clusters can be achieved with relatively high rates of VEGF production and degradation, given the prescribed limits.

Fig. 4(a) illustrates an example of cell clustering produced by the core model using the optimised parameter values given in Table 6, in which 5 clusters are present at $t = 2$. Here one can observe that the
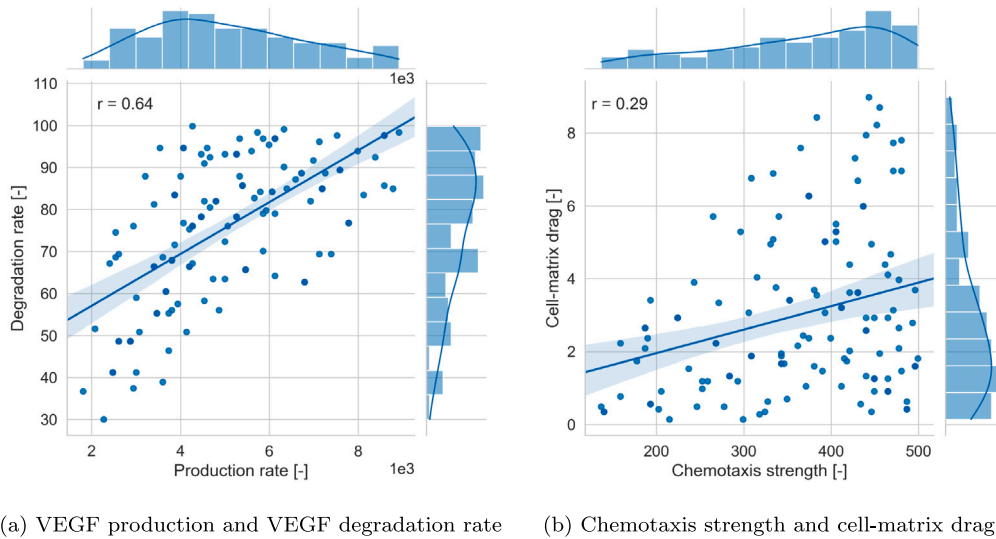
(a) VEGF production and VEGF degradation rate

(b) Chemotaxis strength and cell-matrix drag

**Fig. 2.** Scatter plots showing regression lines for the correlation between parameter values in the data subset that leads to two or more clusters. The Pearson correlation coefficients, denoted $r$, are labelled in boxes on the plots. The marginal plots give the distribution of each parameter value in the data subset as a histogram.
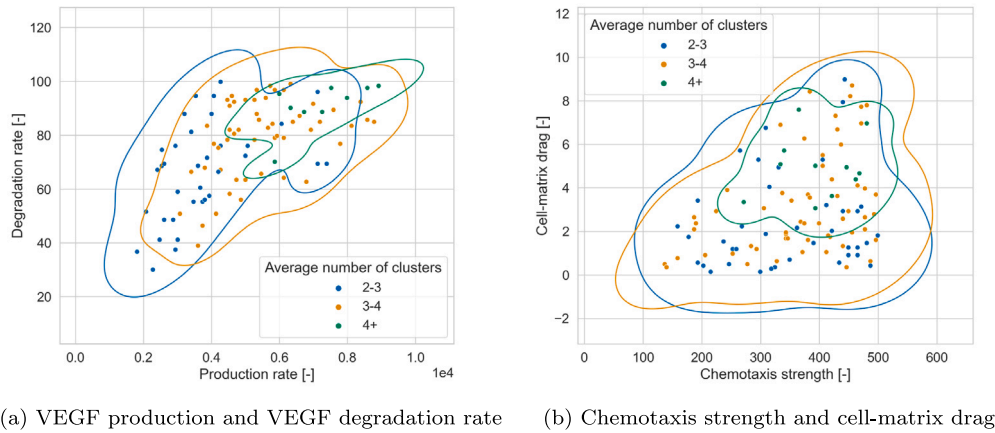


(a) VEGF production and VEGF degradation rate

(b) Chemotaxis strength and cell-matrix drag

**Fig. 3.** Scatter plots where each point is labelled based on the number of clusters formed with those parameter values in the parameter sweep dataset. A KDE (kernel density estimation) contour has been added for each subgroup to highlight the parameter space inhabited by each group.

**Table 7**
Persistence of total number of clusters averaged over 10 initial conditions. Parameter values used were taken from Table 6 ($t = 4$ column).

| $t$ [-] | 2 | 4 | 10 | 20 |
|---|---|---|---|---|
| No. of clusters | 5.9 | 5.5 | 5.1 | 4.6 |

typical spacing between vascular components is at least 350 μm, which is larger than the typical intercapillary distances required for optimal metabolic exchange that are observed *in vitro* and *in vivo* [24]. Fig. 4(b) presents an example of the 2D model output also at $t = 2$ using these parameter values. The spatial scale of the 2D cell structures is similar to the 1D clusters, and this is explored further in Section 5.7.

### 5.3. Long-term behaviour of cell clusters

Based on the optimised parameter values given in Table 6, Table 7 shows the average number of clusters seen at longer time points up to and including $t = 20$. Though the model is currently intended to model initial pattern formation, not long-term cell behaviour, Table 7 demonstrates that patterning driven by autologous chemotaxis in this model can support long-term cell cluster formation.

To illustrate the long-term dynamics of the cell clusters, Fig. 5 presents four examples of cluster persistence, merging, and dissipation that can take place, based on four different random initial conditions. Each example shows the cell volume fraction along the 1D geometry, with time on the *y*-axis up to $t = 20$. In Fig. 5(a), 5 clusters are observed to form between $t = 2.5$ and $t = 5$, before a cluster merging event takes place around $t = 5$ to $t = 7.5$. After $t = 7.5$, four clusters persist appearing stable. Additional analysis is required to conclude whether the system in this case has reached a steady state. Similar merging events take place in Figs. 5(b) and 5(c). In Fig. 5(d), five clusters persist beyond $t = 20$, however there is some displacement of the clusters' positions, indicating that a steady state is not obtained.

### 5.4. Steady state analysis of core model

To understand better these initial findings in terms of optimal core parameters, an analysis of the core model in the steady state is performed. We start with the nondimensional governing Eqs. (14) to (22) without any additional mechanisms ($\kappa = 0$, $K = 0$, $\eta = 0$, $\nu = 0$ and $\delta_n = 0$). By assuming $\frac{\partial}{\partial t} = 0$, $u_n = 0$, and $u_w = 0$, these equations reduce to

$$\frac{\partial}{\partial x}\left(D_u(\phi - n)\frac{\partial c_u}{\partial x}\right) + \alpha n(\phi - n) - \delta c_u = 0, \quad (25)$$

(a) Example cell cluster formation in 1D



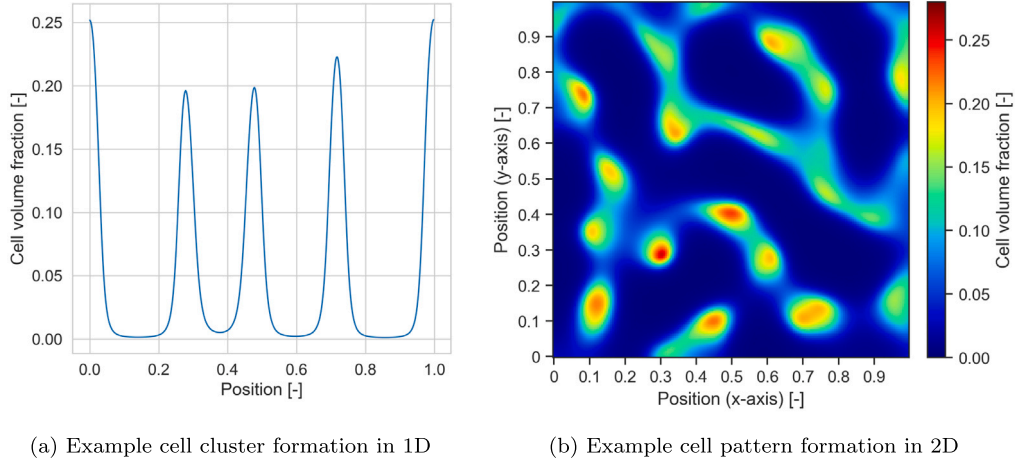(b) Example cell pattern formation in 2D

**Fig. 4.** Example cell cluster and pattern formation for the optimised parameter values given in the first column ($t = 2$) of Table 6, shown at $t = 2$. Dimensionless $L = 1$ corresponds to 3 mm. The same random initial condition was used to generate all 1D and 2D example plots.
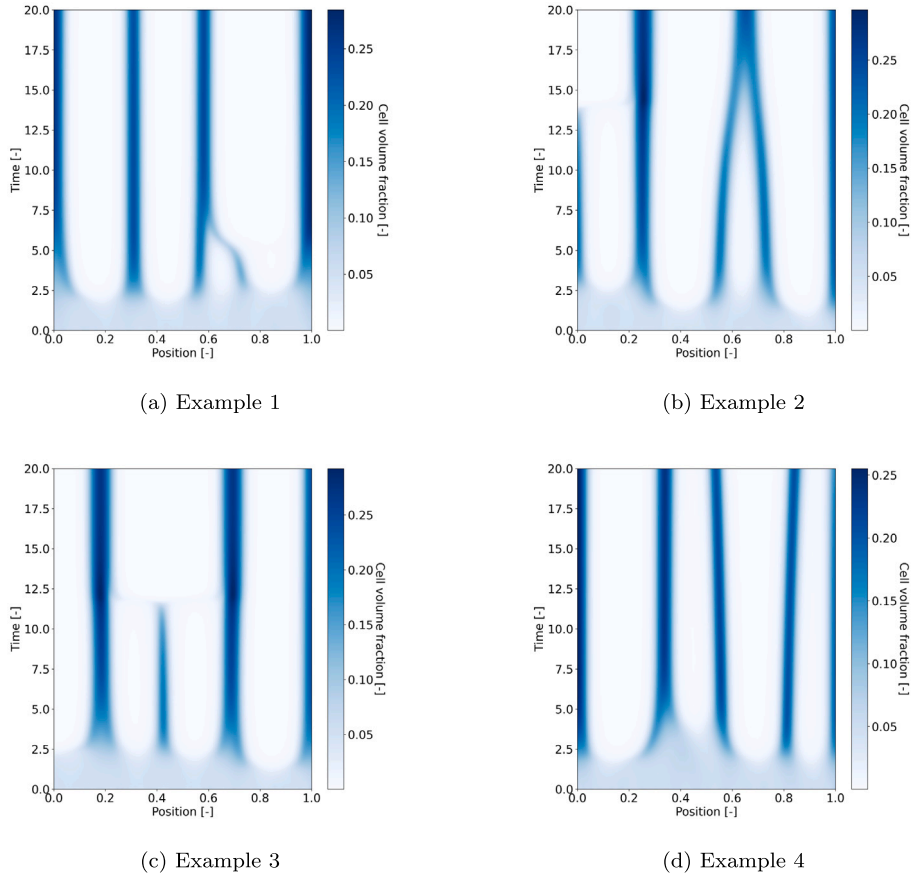


(a) Example 1



(b) Example 2



(c) Example 3



(d) Example 4

**Fig. 5.** Examples of cell cluster persistence and cluster merging over time, using optimised parameter values given in the second column ($t = 4$) of Table 6. Four initial conditions were chosen to reflect the range of long-term behaviours observed.

$$\frac{\partial}{\partial x}\left(n\chi_u \exp\left(-c_u\right)\right) = 0, \tag{26}$$

with $p_w$ constant throughout the domain. To make further progress, it is realistic to assume that the cell population occupies a small volume fraction, so that $n = \epsilon \hat{n}(x)$ with $\epsilon = 0.05 \ll 1$ (also used numerically). A cell cluster lengthscale $X \sim 1$, yet to be determined, is also defined based on $x = \Omega X$ with $\Omega \ll 1$. Applying these assumptions and combining (25) and (26) yields the following leading-order nonlinear ODE for $n(X)$:

$$\hat{n}'' - \frac{(\hat{n}')^2}{\hat{n}} + \hat{\alpha}\hat{n}^2 - \hat{\delta}\hat{n}\left(E + \ln\hat{n}\right) = 0, \tag{27}$$

where $\hat{\alpha} = \alpha\epsilon\Omega^2/D_u$, $\hat{\delta} = \delta\Omega^2/D_u\phi$, and $E = c_u(X) - \ln\hat{n}$ is a constant on the cell cluster lengthscale. A linearised analysis of this equation for small perturbations in cell concentration ($A \ll 0$) suggests a solution of the form

$$\hat{n} \approx \hat{n}_0 + A\cos\left[\left(\hat{\alpha}\hat{n}_0 - \hat{\delta}\right)^{1/2}X\right], \tag{28}$$

so long as $\hat{n}_0 \sim 1$ satisfies $\hat{\alpha}\hat{n}_0 - \hat{\delta}\ln\hat{n}_0 = \hat{\delta}E$, and $\left(\hat{\alpha}\hat{n}_0 - \hat{\delta}\right)^{1/2}$ is restricted to discrete values that satisfy the no-flux boundary conditions at $x = 0$ and 1. Setting our stretched lengthscale to encompass a single cluster
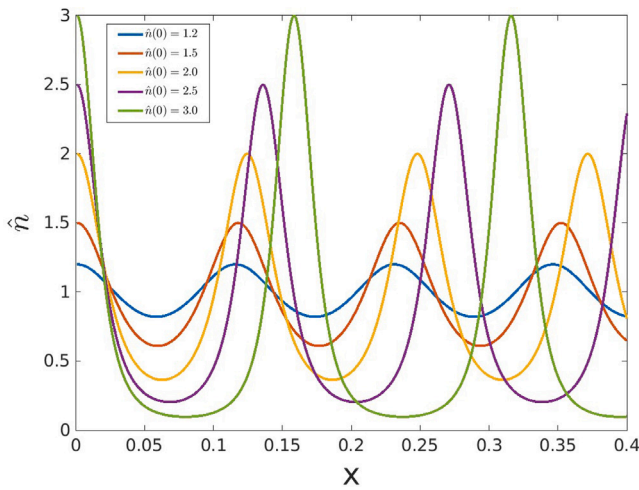
**Fig. 6.** Cell cluster solutions from the steady-state analysis for the following parameter values: $\hat{\alpha} = 4000$, $\hat{\delta} = 1000$, $\hat{n}_0 = 1$, $\epsilon = 0.05$. This shows the solutions obtained by varying the boundary condition $\hat{n}(0)$.

**Table 8**

Dimensionless parameter values of the additional model parameters used to determine which additional parameters may play a role in cell clustering, and the average number of clusters formed over 10 initial conditions at $t = 2$ when each additional parameter is activated individually. The values for other parameters used are as in Table 6 ($t = 2$ column). The number of clusters formed in the core model without additional parameters was 5.9 (Table 7).

| Parameter | First value | No. of clusters | Second value | No. of clusters |
|---|---|---|---|---|
| $\kappa$ | $2 \times 10^4$ | 5.8 | $5 \times 10^4$ | 5.4 |
| $\eta$ | 100 | 5.3 | 200 | 1.9 |
| $\nu$ | 3 | 5.9 | 6 | 5.9 |
| $\delta_n$ | 100 | 5.6 | 200 | 5.5 |

**Table 9**

Dimensionless parameter bounds for the VEGF–matrix binding model parameters used for parameter sweep.

| Parameter | Minimum value | Maximum value |
|---|---|---|
| $\chi_u$ | 0 | 500 |
| $\chi_b$ | 0 | 500 |
| $\gamma_{nm}$ | 0.1 | 10 |
| $\alpha$ | $1 \times 10^3$ | $9 \times 10^3$ |
| $\delta$ | 10 | 100 |

$(X \sim 1)$ suggests

$$\Omega = 2\pi \left( \frac{D_u}{\alpha \hat{n}_0 \epsilon \phi - \delta} \right)^{1/2}$$

as a nondimensionalised cell cluster lengthscale based on VEGF production and degradation rates. Using the optimal values at $t = 2$ from Table 6 with $\epsilon \hat{n}_0 = 0.05$ yields $\Omega \approx 0.12$ which, in dimensional units, is comparable to that observed in the computational results ($\sim 350$ μm). As the perturbations become larger and nonlinear, numerical computations of (27) indicate that the cluster width remains approximately constant and equal to $\Omega$ (Fig. 6). The gaps between clusters, however, become larger as the nadir approaches zero, thus reducing the overall number of clusters that can exist within the fixed domain.

Fig. 7(a) shows an attempt to replicate the numerical results (shown in Fig. 7(b)) based on the optimal parameters at $t = 2$ in Table 6; two important observations can be made from this comparison. The first is that the perturbation required to reproduce the cluster pattern obtained numerically is close to the maximum perturbation threshold that can yield a periodic solution; this could have implications on controlling this process. The second observation is that, while the analysis reproduces the cluster shapes and gap spacing very well, the computational model produces clusters of slightly differing amplitudes, particularly those adjacent to the walls. On closer examination of the numerical results, the cause of the differing amplitudes is almost certainly down to the fact that the computations at $t = 2$ have not yet fully reached a steady state. As a result, the mean cell volume concentration $\hat{n}_0$ is not uniform across the domain, as assumed in the steady-state analysis, generating differing cluster heights locally around a location $a$ for $(x - a)/\Omega \sim 1$. The distinctly larger amplitudes close to the boundaries (near $x = 0$ and $x = 1$) are very likely caused by cell accumulation as a consequence of the no-flux boundary conditions, leading to larger values of $\hat{n}_0$ locally.

### 5.5. Impact of additional mechanisms on cell cluster formation

Given the limits of the core model investigated, in which the minimum spatial scale of patterning was found to be $\sim 350$ μm, some common additional mechanisms are considered to determine their potential impact on this patterning scale. These include: (i) VEGF uptake, (ii) cell–matrix traction, (iii) cell–cell aggregation, and (iv) cell–cell contact inhibition (previously all set to zero).

The first additional mechanism, VEGF uptake, is characterised by two parameters (see Section 2.3.5): an uptake rate, $\kappa$, and the VEGF

concentration at which uptake is half-maximal, $K$. The second, cell-matrix traction, is an additional interphase force in Eqs. (21) and (22), characterised by the traction force parameter $\eta$. The final two, aggregation and contact inhibition, are included as cell intraphase pressures in the additional pressure term $\Pi_n$ shown in the general Eq. (5), and expanded in Eqs. (21) and (22). These two mechanisms are characterised by the parameters $\nu$, a cell–cell aggregation pressure, and $\delta_n$, a cell–cell contact inhibition pressure.

To determine the impact that each of these parameters has on the spatial scale of pattern formation in the model, the number of cell clusters produced under the same core parameter regime and initial conditions was determined for a range of values of these additional parameters. The dimensionless parameter values considered for each are shown in Table 8. Table 8 also presents the average number of cell clusters formed in each case, averaged over the same 10 initial conditions as used previously. While these additional parameters exert some influence on the number of clusters formed, they are unable to increase the number of clusters any further and hence reduce the spatial scale of patterning observed. Fig. 8 further illustrates the limited influence of each of these parameters, using a fixed initial condition and core parameter values, in both 1D and 2D.

### 5.6. Impact of VEGF-matrix binding on patterning scale

Motivated by reducing the spatial scale of pattern formation, we consider the inclusion of VEGF–matrix binding on cell cluster and pattern formation. Given that parameter values for the binding rates $k_b$ and $k_u$ are fixed, based on [40], the binding model is treated as an alternate model choice to the core model analysed so far, and may require different core parameter values.

Similarly to the core model, a parameter sweep was first conducted: a Saltelli sampler was used to generate 896 parameter samples using the dimensionless parameter bounds given in Table 9. The VEGF–matrix binding model achieved a much higher average number of clusters, up to 10, compared to the maximum average of 4.7 observed the core model.

Fig. 9 presents three notable relationships between parameters in this subset, based on correlation coefficient values. Compared to the core model, VEGF production rate and degradation rate are less closely linked, and there is no evident correlation between the magnitude of these parameters and the number of clusters formed (Fig. 9(a)). Though the values of degradation rate in this subset are skewed toward higher values, plotted as a marginal histogram in Fig. 9(b), it is evident
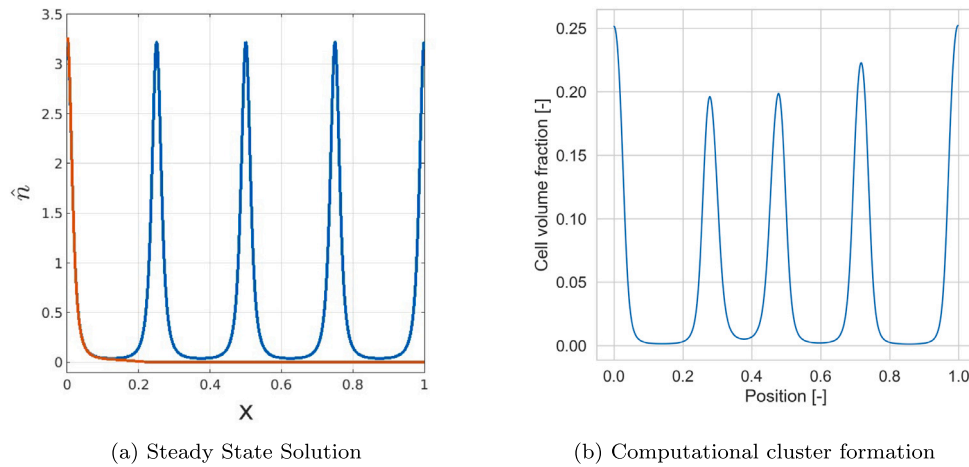
(a) Steady State Solution



(b) Computational cluster formation

**Fig. 7.** Example cell cluster and pattern formation for the optimised parameter values given in the first column ($t = 2$) of Table 6, shown at $t = 2$. This shows the computational result obtained side-by-side with a steady-state analysis solution using the same parameters. Plot (a) also shows a second solution (red line) obtained from (27) using a slightly higher value of $\hat{n}$ at $x = 0$ which fails to produce any periodic behaviour.

**Table 10**
Dimensionless parameter values found to maximise the number of cell clusters produced by the VEGF–matrix binding model at $t = 2$ and $t = 4$ respectively, using the particle swarm optimisation method.

| $t$ [-] | 2 | 4 |
|---|---|---|
| average no. of clusters | 9.3 | 8.0 |
| VEGF degradation rate | 82.1 | 33.2 |
| VEGF production rate | $8.74 \times 10^3$ | $4.11 \times 10^3$ |
| Cell-matrix drag | 8.90 | 6.81 |
| Chemotaxis strength (bound) | 424 | 497 |
| Chemotaxis strength (unbound) | 13.6 | 90.4 |

**Table 11**
Total Sensitivity indices for each of the parameters in the extended VEGF–matrix binding model, based on the number of cell clusters formed, at $t = 1, 2, 3,$ and 4 respectively.

| $t$ [-] | 1 | 2 | 3 | 4 |
|---|---|---|---|---|
| VEGF degradation rate | 0.63 | 0.61 | 0.63 | 0.64 |
| VEGF production rate | 0.49 | 0.46 | 0.45 | 0.41 |
| Chemotaxis strength (unbound) | 0.52 | 0.32 | 0.26 | 0.26 |
| Chemotaxis strength (bound) | 0.50 | 0.39 | 0.36 | 0.32 |
| Cell-matrix drag | 0.23 | 0.24 | 0.22 | 0.19 |
| Rate of binding | 0.08 | 0.08 | 0.09 | 0.09 |
| Rate of unbinding | 0.11 | 0.12 | 0.12 | 0.13 |

from the scatter and kernel density estimate (KDE) plot that as the chemotaxis strength for bound VEGF increases, there is a greater spread of degradation rates. This suggests that for high bound chemotaxis strength values, the model is less sensitive to the VEGF degradation rate.

Finally, Fig. 9(c) demonstrates the spread of values for bound and unbound chemotaxis strength in this subset. The marginal histograms show that there is a skew towards high values of bound chemotaxis strength, but not unbound chemotaxis strength, suggesting the model is less sensitive to the latter in the binding model. The scatter/KDE plot suggests that the highest number of clusters, greater than 8, generally requires a relatively high bound chemotaxis strength and relatively low unbound chemotaxis strength.

To verify the maximum number of cell clusters that can be formed in the 1D binding model, a parameter optimisation using particle swarm optimisation was conducted. The parameter values found to maximise the number of clusters forming, averaged over 10 initial conditions as in the core model analysis, are given for $t = 2$ and $t = 4$ in Table 10. At both $t = 2$ and $t = 4$, the optimal parameter values were found to be for relatively low unbound chemotaxis strength, and relatively high chemotaxis strength to bound VEGF, as suggested by the parameter sweep findings in Fig. 9. Moreover, the parameter values found for VEGF production and degradation rate for $t = 4$ support that high values for these parameters are not strictly necessary for a large number of clusters to form unlike in the core model.

The findings of the above parameter sweep and particle swarm optimisation appear to suggest that including VEGF–matrix binding leads to a more robust simulation outcome against variation in VEGF production and degradation rates. To investigate this hypothesis, a sensitivity analysis was performed on the VEGF–matrix binding model parameters based on the chemotaxis, cell-matrix drag, production and degradation upper and lower bounds given in Table 9, as well as the

upper and lower bounds for the rate of binding and unbinding given by Köhn-Luque et al. [40]. The results of the sensitivity analysis are shown in Table 11, where the influence of the strength of chemotaxis to bound VEGF at $t = 4$ is higher than for the strength of chemotaxis to free VEGF. All other parameters exhibit a similar influence as in the core model, though the $S_i$ values for VEGF production and degradation are lower than those obtained for the core model ( Table 5) as predicted. The low $S_i$ values for the rates of binding and unbinding confirm that the experimental upper and lower bounds are sufficiently narrow that the uncertainty in these parameters do not overshadow the impact of the other model parameters on the model outcome.

Fig. 10 illustrates cell clustering produced by the VEGF–matrix binding model using the optimised parameter values in Table 10. Fig. 10(b) both confirms the ability of the extended VEGF–matrix binding model to generate connected vascular-like structures on a biologically relevant timescale, and indicates that the VEGF–matrix binding model can better match the spatial scale of vascular network formation as indicated by the 1D analysis.

Motivated by findings in previous chemotaxis-driven models [24, 41], Fig. 11 presents the binding model with alternate initial cell volume fraction (0.04 or 0.06 compared to 0.05). For the higher cell volume fraction, a more connected structure is generated, moving towards a 'swiss cheese' pattern as opposed to disconnected vascular-like segments. This patterning also required a longer time to form (t = 3 as opposed to t = 2). However, initial cell volume fractions greater than 0.06 prevented vascular-like patterning (data not shown).

### 5.7. Quantification of spatial scale and connectivity

Here we present statistics for cluster (1D) and vessel segment (2D) spacings to compare to the patterning size seen *in vitro* on the order of
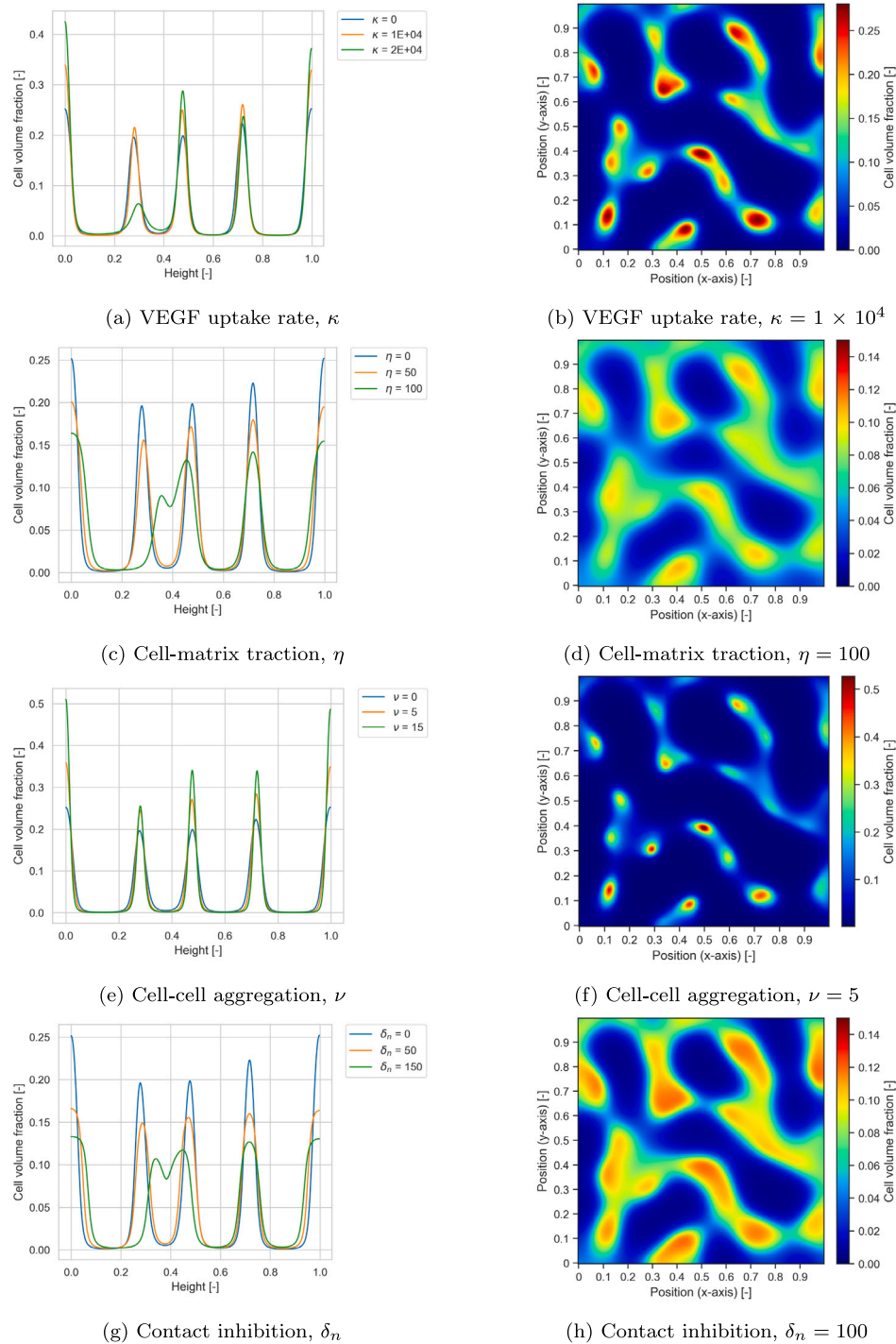
(a) VEGF uptake rate, $\kappa$



(b) VEGF uptake rate, $\kappa = 1 \times 10^4$



(c) Cell-matrix traction, $\eta$



(d) Cell-matrix traction, $\eta = 100$



(e) Cell-cell aggregation, $\nu$



(f) Cell-cell aggregation, $\nu = 5$



(g) Contact inhibition, $\delta_n$



(h) Contact inhibition, $\delta_n = 100$

**Fig. 8.** Examples of the impact of additional parameters in 1D and 2D, each shown at $t = 2$. The core parameter values used were fixed based on Table 6, and the same initial condition was used to generate each example.

200 μm. We further consider additional network-related metrics in the 2D case to assess branching, connectivity, and lacunae presence and diameter. The computational methods used to obtain these metrics a outlined in Section 4.1.1.

*5.7.1. Patterning spatial scale*

To confirm the typical spatial scale of the core and binding models, the width and spacing of each cell structure formed were assessed for each 1D model over 10 random initial conditions. In Fig. 12, the distribution of metrics in the 1D core model is compared with the metrics in the 1D binding model. This demonstrates a significant reduction in both metrics (p < 0.001), particularly in cluster spacing

which is of the most interest. For the 1D binding model, the average cluster spacing was found to be 229 μm, of the same order of vessel separation observed *in vitro* [24].

Fig. 13 makes a similar comparison for the 2D core and 2D binding models, with clear reduction in both metrics for the binding model (p < 0.001). Compared to 1D, each metric average appears slightly larger, likely due to the method employed to determine these metrics. In 2D, the metrics were determined by taking several 1D slices in each dimension, however this does not guarantee to pass through the most narrow part of each network segment, nor capture the smallest separation of segments, leading to the larger spread of measurements
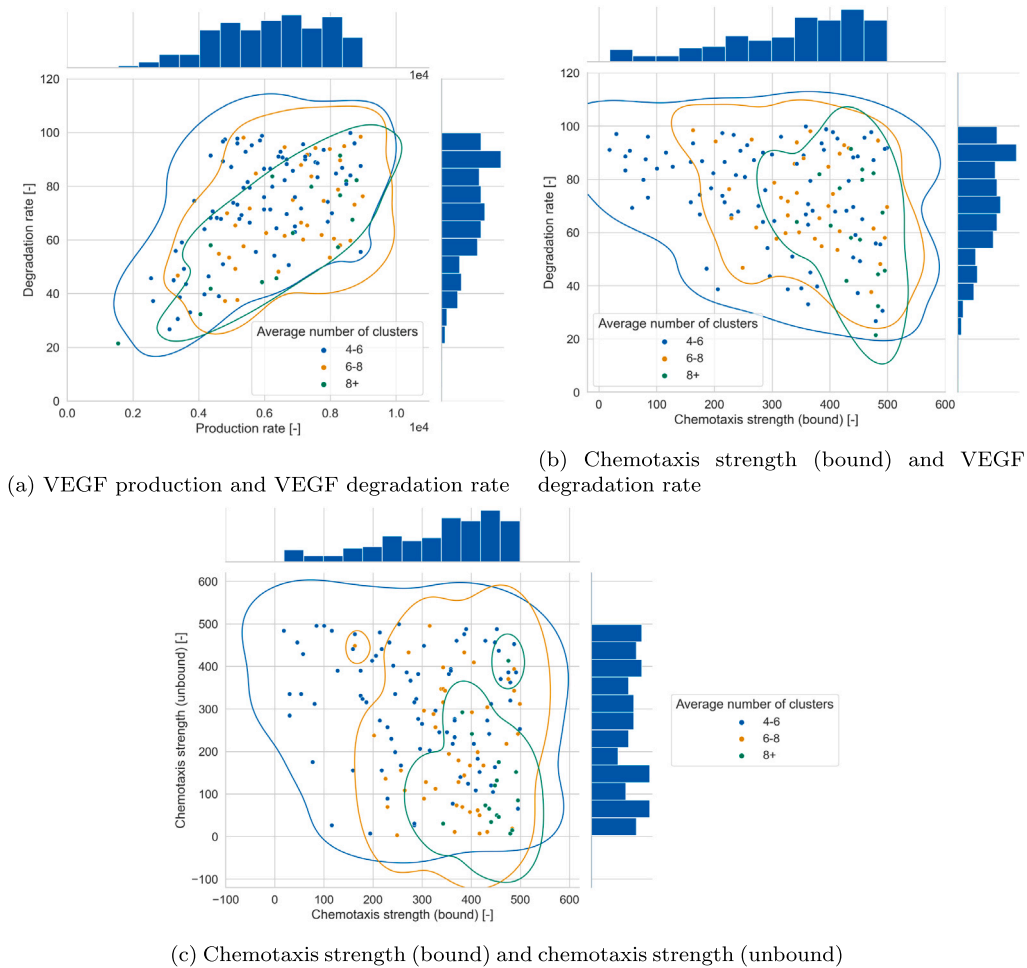
(a) VEGF production and VEGF degradation rate

(b) Chemotaxis strength (bound) and VEGF degradation rate

(c) Chemotaxis strength (bound) and chemotaxis strength (unbound)

**Fig. 9.** Labelled scatter and kernel density estimate (KDE) plots showing the parameter values in the sweep that obtained either 4–6, 6–8, or more than 8 clusters at $t = 2$. The relationships between VEGF production rate, VEGF degradation rate, and both chemotaxis strength parameters are included as these had the highest correlation coefficient in the data subset. The marginal plots give a histogram distribution for each of these parameters in the data subset.



(a) Example cell cluster formation in 1D

(b) Example cell pattern formation in 2D
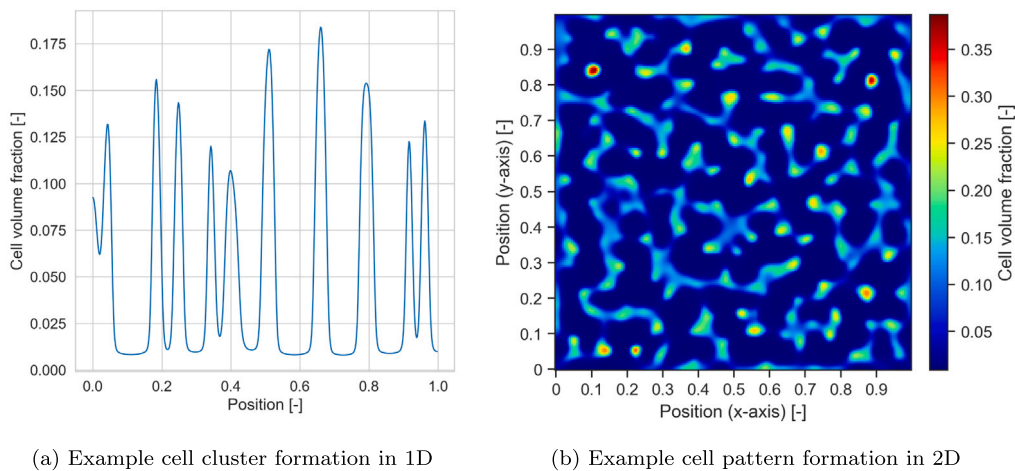
**Fig. 10.** Example cell cluster and pattern formation for the VEGF–matrix binding model with the optimised parameter values given in the first column ($t = 2$) of Table 10, shown at $t = 2$. Dimensionless L = 1 corresponds to 3 mm. The same random initial condition was used to generate all 1D and 2D example plots.

(a)       (b)       (c)
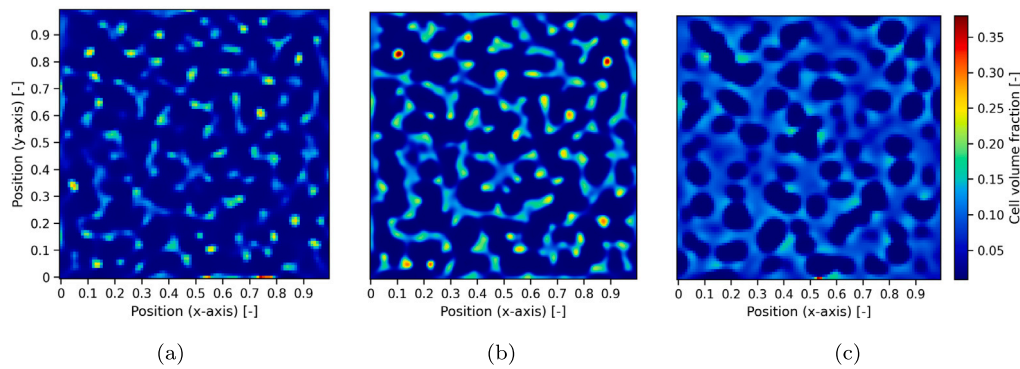
**Fig. 11.** Example pattern formation for the VEGF–matrix binding model, for average cell volume fraction of (a) 0.04 at $t = 1.5$, (b) 0.05 at $t = 2$, and (c) 0.06 at $t = 3$. The parameter values used are given in the first column ($t = 2$) of Table 10. Dimensionless L = 1 corresponds to 3 mm. The same random initial condition was used to generate all 1D and 2D example plots.
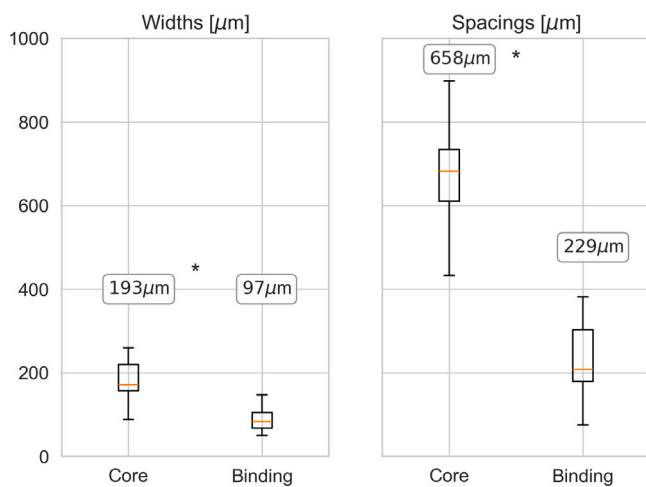


**Fig. 12.** Spatial metrics for 1D core and 1D binding model, using optimised parameter values. The metrics were extracted from 10 simulations given random initial conditions. The mean values are given, and the asterisks denote significance.
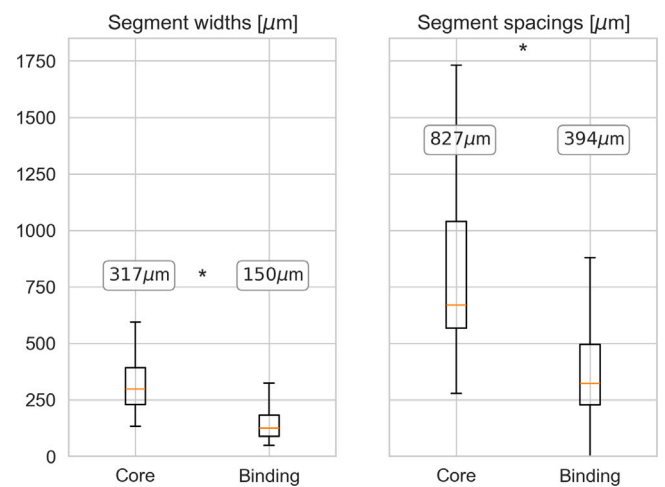


**Fig. 13.** Spatial metrics for 2D core and 2D binding model, using optimised parameter values. The metrics were extracted from 10 simulations given random initial conditions. The mean values are given, and the asterisks denote significance.

for the 2D metrics. The additional impact of initial cell volume fraction on these metrics is shown in Appendix B.

#### 5.7.2. 2D network metrics

In 2D, it is more appropriate to treat the vascular-like patterning as a network to quantify branching, average branch length, network connectivity, and the size of any lacunae. Fig. 14 illustrates the increase in the number of branches per node, and decrease in branch width, as the network becomes more complex with the addition of VEGF–matrix binding. No lacunae were identified in any of the core model outputs analysed, and the binding model outputs had an average of two lacunae per network and maximum of six, with average diameter of 300 μm.

Where the network is not strongly connected, i.e. not every node can be reached from every other node, we can consider average node connectivity: for each pair of nodes, we take the maximum number of disjoint paths connecting them, and take the average for all pairs of nodes in the graph. Fig. 15 shows that this average connectivity is slightly higher in the binding model, but significantly higher with an increased average cell volume fraction (0.06 compared to 0.05). Indeed, 8 out of 10 networks produced with the higher initial cell density were strongly connected, which was not true of any of the networks with the lower cell density. Further analysis may be beneficial to optimise cell volume fraction alongside the model parameter values, and assess their interdependence.

### 6. Conclusion

In this paper, we have demonstrated the potential for the multiphase model framework to be used to simulate cell patterning in 1D and 2D, including the formation of cell clusters and of vascular-like structures. We have investigated cell mechanisms commonly included in models of vascular network formation and more general multiphase models, with a focus on the influence of each parameter on the spatial and temporal scale of patterning. Using sensitivity analysis, four core parameters were identified and demonstrated to enable the formation of cell clusters and vascular-like structures in 1D and 2D respectively, on a biologically plausible timescale (2 to 4 days). A steady-state asymptotic analysis reinforced the findings of the numerical core model results, particularly in terms of the expected cluster width and cluster spacing being strongly influenced by VEGF production and degradation rates. Additional model mechanisms, including cell–matrix traction, VEGF uptake, cell–cell aggregation, and cell contact inhibition, were not found to favourably reduce the spatial scale of cluster formation. Alternatively, the addition of VEGF–matrix binding as a model extension was found to match the spatial scale of patterning as observed *in vitro*, with significantly smaller pattern spacing compared to the core model.
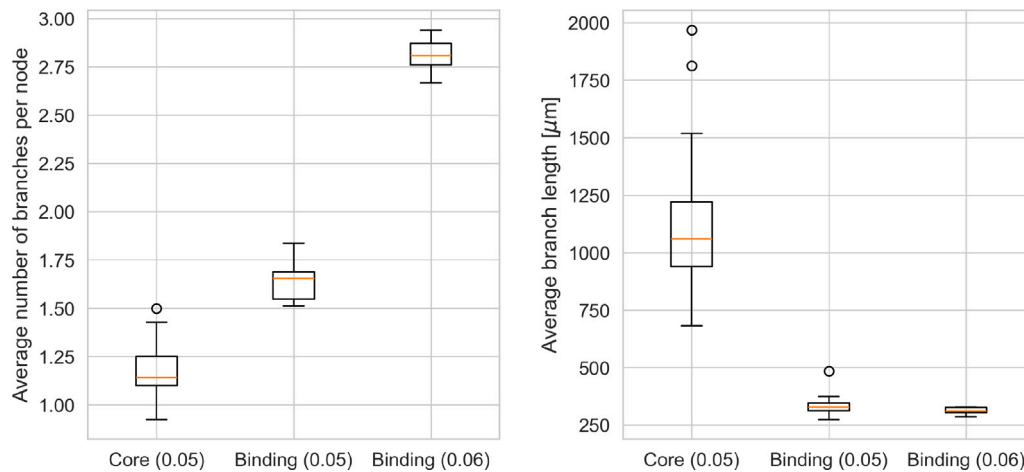
**Fig. 14.** Number of branches per node and length of branches for 2D core and 2D binding model, with initial cell volume fraction of either 0.05 or 0.06, using optimised parameter values. The metrics were extracted from 10 simulations given random initial conditions.
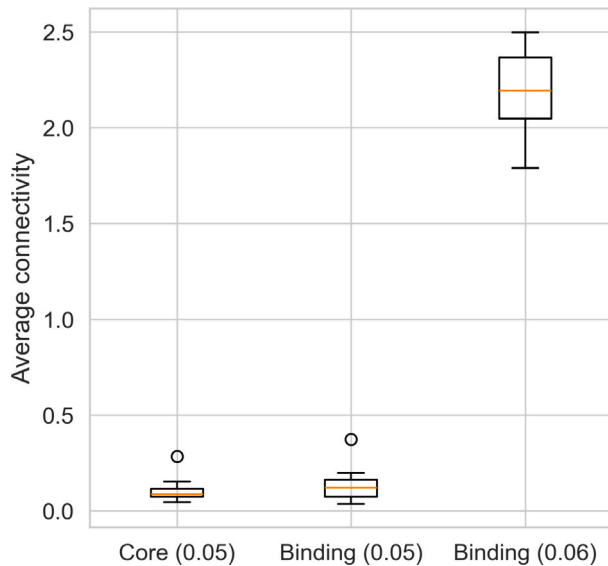


**Fig. 15.** Average connectivity of networks in the core and binding models, with average cell volume fraction of either 0.05 or 0.06, using optimised parameter values. The metrics were extracted from 10 simulations given random initial conditions.

In this analysis, we have demonstrated that the combination of analyses methods employed here: parameter sweep, sensitivity analysis, steady-state asymptotics, and parameter optimisation is an efficient way to guide the optimisation of the 2D vascular network formation model. Furthermore, the sensitivity analysis identified an increase in robustness of the binding model to some of the core parameters, particularly for VEGF production and VEGF degradation.

Future analysis may include the application of some of these computational techniques, including parameter optimisation, to the 2D model directly. Additionally, the analysis would benefit from a much deeper look at persistence of the vascular-like structures in 2D, and the stability of metrics observed over a longer time point. To adapt the model presented here to long-term behaviour, it is likely that additional stabilising mechanisms such as a temporal-dependence on the cell-matrix interactions, driven by augmentation of the matrix distribution by the cells, may be required to match *in vitro* findings. Cell matrix degradation is often observed in the initial stages of network formation, aiding cell migration, and then an increase in deposition of ECM components including laminin and collagen IV is observed in the latter stages [63,64]. Whereas collagen is seen to increase cell migration, these basement membrane proteins serve to stabilise capillary structures. A first, simplified model of this behaviour may consider cell-derived deposition of proteins that directly replace the existing collagen matrix, such that two main proteins constitute the constant $m$, each with different mechanical and chemical properties.

The impact of initial or average cell volume fraction (equal in the absence of proliferation), was considered briefly here and shown to positively affect the connectivity of the resulting 2D network. The sensitivity of the network properties to the cell volume fraction, particularly in relation to variable parameter values, would be of value to assess. Here, cell volume fraction was not considered as a variable alongside the parameter values, and hence the sensitivity and optimisation of the parameter values are limited to a particular initial cell volume fraction.

Overall, this study has demonstrated potential for the multiphase model to capture key *in vitro* behaviours at the time points considered, which makes it a prime candidate for further development to be utilised alongside experimental studies. In particular, the wide range of experimental variables associated with *in vitro* vascular network formation can be quantitatively assessed computationally by sensitivity analysis, as well as analytically via asymptotic analysis, to determine the most influential on the emerging network structure and topology. The adoption of computational analyses, such as demonstrated here, has the power to significantly reduce the experimental load towards *in vitro* development of vascularised engineered tissues and accelerate research in this area towards clinical application.

**CRediT authorship contribution statement**

**Georgina al-Badri:** Writing – review & editing, Writing – original draft, Visualization, Validation, Software, Methodology, Formal analysis, Conceptualization. **James B. Phillips:** Writing – review & editing, Validation, Supervision, Conceptualization. **Rebecca J. Shipley:** Writing – review & editing, Supervision, Methodology, Conceptualization. **Nicholas C. Ovenden:** Writing – review & editing, Validation, Supervision, Project administration, Methodology, Conceptualization.

**Declaration of competing interest**

The authors have no conflict of interest to declare.

**Data availability**

The code used to solve the multiphase model and produce the figures in the manuscript is available in a GitHub repository.

## Appendix A. Numerical methods and verification

### A.1. Model solver

Backward-time and central-space (BTCS) finite differences have been applied to the model equations, and boundary conditions implemented by adopting a forward- or backward-space difference on the boundary, as appropriate. With the BTCS method, it has been previously shown that upwinding is not required for advection terms [65]. For further confirmation, a version of the code where upwinding was used for Eq. (14) was tested and found to produce near-identical results to the BTCS method.

The resulting set of coupled matrix problems were solved algorithmically within each timestep with use of Python's inbuilt linear algebra solvers. Listing 1 gives an outline of the algorithmic approach to the numerical implementation to solve each matrix problem in sequence. In order to decouple the equations, the assumption is made that the cell velocity components $u_n$ and $v_n$ do not change significantly between timesteps, verified to be true for the timestep size used for the simulations. This enables the cell volume fraction equation to be solved first, and enables decoupling of the two cell momentum equations to solve $u_n$ and $v_n$ separately.

```python
def Timestep(cell, solute, bound_solute,
    water, grid, dt):

    """
    Updates all variable distributions to
    advance the model by a single timestep.

    Inputs
    ----------
    cell : Cell object
    solute : Solute object
    water : Water object
    grid : Grid object
    dt : timestep (float)

    """

    # update cell distribution
    cell.distribution = cell_solver(cell,
    grid)

    # use no voids constraint to update
    water distribution
    water.distribution = phi - cell.
    distribution

    # update water pressure
    water.pressure = pressure_solver(water,
    grid)

    # update water velocity
    water.velocity = water_velocity_solver(
    water, grid)

    # update unbound and bound VEGF
    distribution (where applicable)
    solute.distribution = solute_solver(
    solute, bound_solute, cell, water, grid)
```

```python
    # update cell velocities
    cell.velocity = cell_velocity_solver(
    cell, solute, bound_solute, grid)

    # check for volume conservation and
    consistency
    if negative values occur in cell, water,
     or solute distributions:
        raise ValueError('Negative volume
    fraction in cell, water or solute
    distributions')
    assert (water.distribution + cell.
    distribution + m).all() == 1
    assert sum(cell.previous_distribution)
    == approx(sum(cell.distribution))
    return
```

**Listing 1:** Algorithm for sequential application of matrix solvers within each timestep.

### A.2. Numerical verification

The grid- and time-step convergence for the BTCS implementation is verified here for the 1D and 2D Cartesian binding models. By comparing numerical solutions to a 'ground truth' solution, approximated by a highly accurate numerical solution obtained by using a very fine grid and/or very small timestep, it is expected that errors in the BTCS scheme are of order 2 in space and of order 1 in time. The numerical scheme was tested and convergence plots are presented here using parameter values identified as optimal for pattern formation in the binding model, given in Table 10 in Section 5.6. These parameter values are selected as they represent the most extreme values in terms of the complexity of the simulation results, and so are most suitable to test the robustness of the numerical implementation.

Figs. A.16(a) and A.18(a) show that the error related to grid size is of order 2 in both the 1D and 2D Cartesian model implementations as expected, where the red line has gradient 2. Figs. A.17(a) and A.19(a) show that the error related to increasing timestep size is of order 1 as expected, where the red line has gradient 1. Due to lower computational expense, it is possible to run the 1D model on a finer grid, to obtain a more accurate ground truth solution against which the errors are calculated. The ground truth solution adopted for the 2D grid convergence plot (Fig. A.18(a)) is based on a coarser grid, hence the errors for solutions with grid sizes close to the ground truth grid size tend towards negative infinity on the log scale, and the error curve bends downwards slightly. However, it is clear accumulative errors relating to increasing grid spacing and timestep are relatively small; the maximum cell volume fraction conservation error seen during verification testing was 0.035%.

## Appendix B. Impact of initial cell volume fraction on cluster formation

### B.1. 1D core model

See Fig. B.20.

### B.2. 1D binding model

See Fig. B.21.

(a) Grid convergence
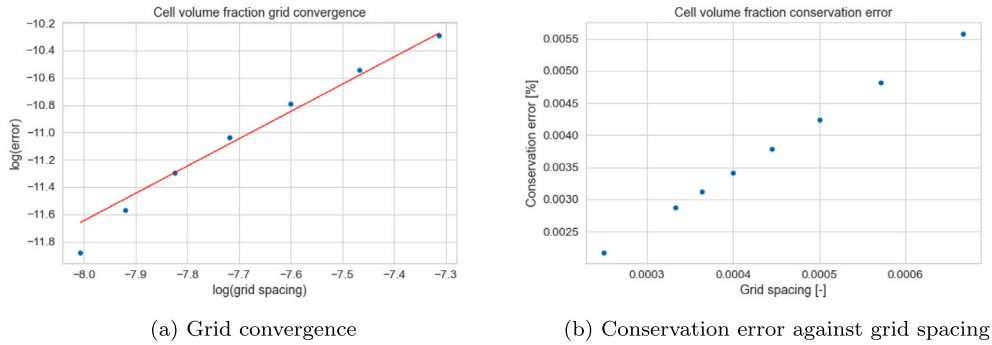


(b) Conservation error against grid spacing

**Fig. A.16.** 1D Cartesian code convergence plots (grid spacing). The red line in Fig. A.16(a) is of gradient 2 through one of the data points. The parameter values used are those found by parameter optimisation, given in Table 10. The grid spacing ranged from $dx = 2.5 \times 10^{-4}$ to $dx = 6.7 \times 10^{-4}$. The timestep was fixed at $dt = 0.002$, and the errors were calculated at $t = 0.2$.
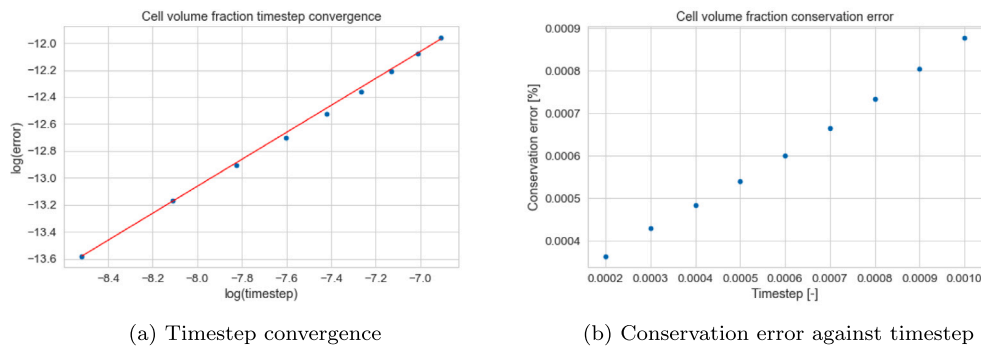


(a) Timestep convergence



(b) Conservation error against timestep

**Fig. A.17.** 1D Cartesian code convergence plots (timestep). The red line in Fig. A.17(a) is of gradient 1 through one of the data points. The parameter values used are those found by parameter optimisation, given in Table 10. The timestep ranged from $dt = 1 \times 10^{-4}$ to $dt = 1 \times 10^{-3}$. The grid spacing was fixed at $dx = 3.3 \times 10^{-4}$, and the errors were calculated at $t = 0.2$.
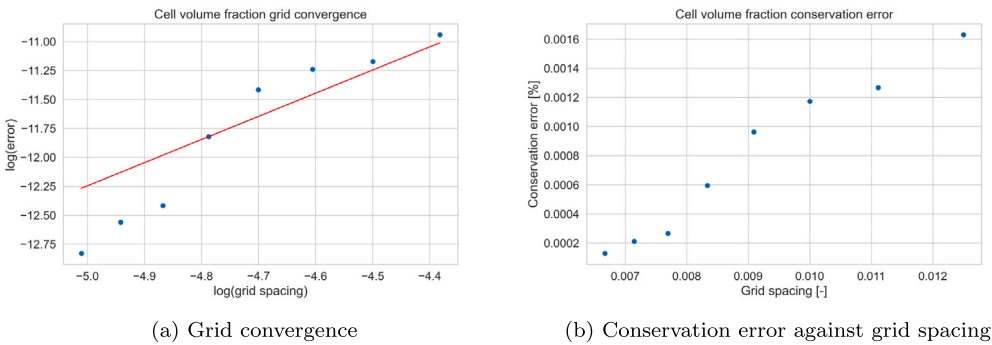


(a) Grid convergence



(b) Conservation error against grid spacing

**Fig. A.18.** 2D Cartesian code convergence plots (grid spacing). The red line in Fig. A.18(a) is of gradient 2 through one of the data points. The parameter values used are those found by parameter optimisation, given in Table 10. The grid spacing ranged from $dx = 5 \times 10^{-3}$ to $dx = 1.25 \times 10^{-2}$. The timestep was fixed at $dt = 5 \times 10^{-4}$, and the errors were calculated at $t = 0.1$.
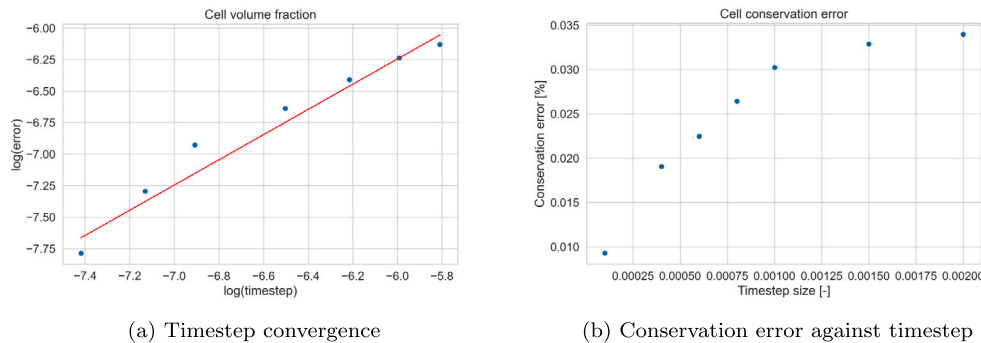


(a) Timestep convergence



(b) Conservation error against timestep

**Fig. A.19.** 2D Cartesian code convergence plots (timestep). The red line in Fig. A.19(a) is of gradient 1 through one of the data points. The parameter values used are those found by parameter optimisation, given in Table 10. The timestep ranged from $dt = 1 \times 10^{-4}$ to $dt = 1 \times 10^{-3}$. The grid spacing was fixed at $dx = 8.3 \times 10^{-3}$, and the errors were calculated at $t = 0.1$.
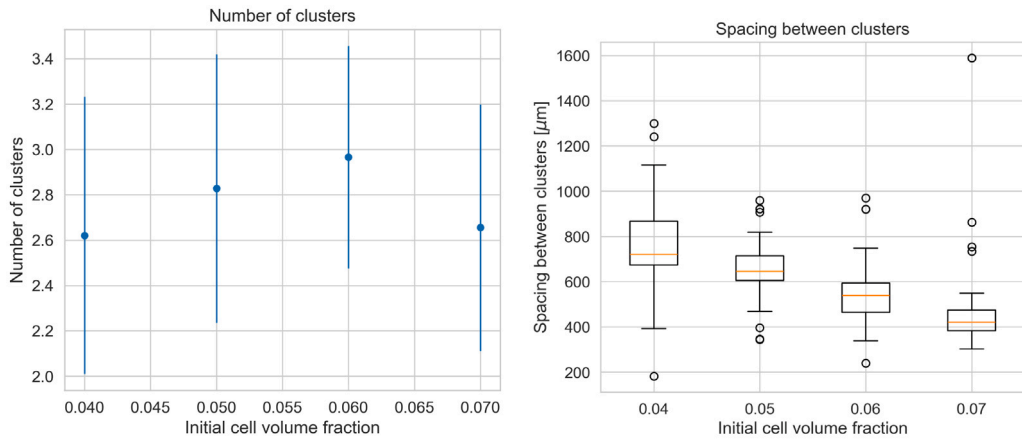
(a) Number of clusters against initial cell volume fraction

(b) Cluster spacing against initial cell volume fraction

**Fig. B.20.** Impact of initial cell volume fraction on the number of clusters and cluster spacing observed in the 1D core model. The parameter values are those found in optimisation and given in Table 6.
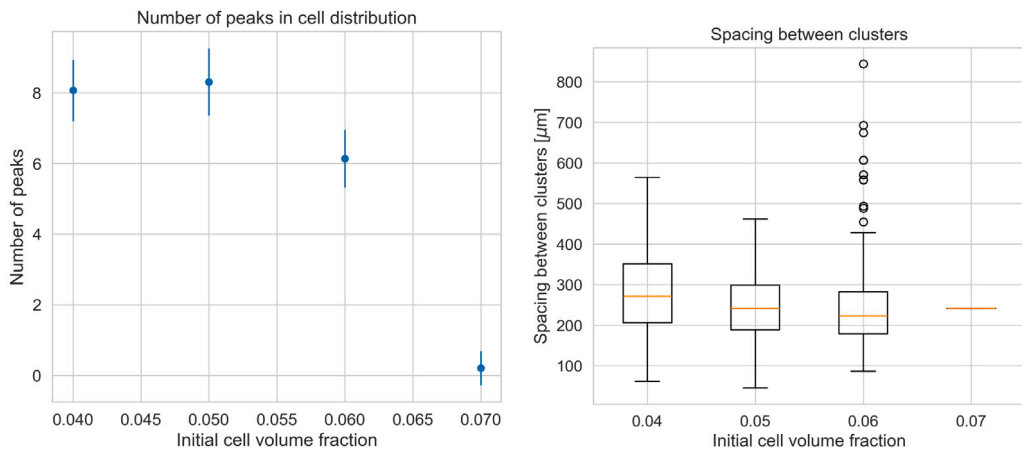


(a) Number of clusters against initial cell volume fraction

(b) Cluster spacing against initial cell volume fraction

**Fig. B.21.** Impact of initial cell volume fraction on the number of clusters and cluster spacing observed in the 1D binding model at $t = 2$. The parameter values are those found in optimisation and given in Table 10.

## References

[1] Katharine R. Bittner, Juan M. Jiménez, Shelly R. Peyton, Vascularized biomaterials to study cancer metastasis, Adv. Healthcare Mater. 9 (8) (2020) 1901459.

[2] Pierre Luc Tremblay, Valérie Hudon, François Berthod, Lucie Germain, François A. Auger, Inosculation of tissue-engineered capillaries with the host's vasculature in a reconstructed skin transplanted on mice, Am. J. Transplant. 5 (5) (2005) 1002–1010.

[3] Yu I. Shen, Hongkwan Cho, Arianne E. Papa, Jacqueline A. Burke, Xin Yi Chan, Elia J. Duh, Sharon Gerecht, Engineered human vascularized constructs accelerate diabetic wound healing, Biomaterials 102 (2016) 107–119.

[4] H.H. Greco Song, Rowza T. Rumma, C. Keith Ozaki, Elazer R. Edelman, Christopher S. Chen, Vascular tissue engineering: Progress, challenges, and clinical promise, in: Cell Stem Cell, vol. 22, (no. 3) Cell Press, 2018, pp. 340–354.

[5] Guang Yang, Bhushan Mahadik, Ji Young Choi, John P Fisher, Vascularization in tissue engineering: Fundamentals and state-of-art, Progr. Biomed. Eng. 2 (1) (2020) 012002.

[6] Timo Rademakers, Judith M. Horvath, Clemens A. van Blitterswijk, Vanessa L.S. LaPointe, Oxygen and nutrient delivery in tissue engineering: Approaches to graft vascularization, J. Tissue Eng. Regenerat. Med. 13 (10) (2019) 1815–1829.

[7] William G. Chang, Laura E. Niklason, A short discourse on vascular tissue engineering, npj Regenerat. Med. 2 (1) (2017).

[8] M. Scianna, C.G. Bell, L. Preziosi, A review of mathematical models for the formation of vascular networks, J. Theoret. Biol. 333 (2013) 174–209.

[9] S.L. Waters, L.J. Schumacher, A.J. El Haj, Regenerative medicine meets mathematical modelling: Developing symbiotic relationships, Npj Regenerat. Med. 6 (1) (2021) 1–8.

[10] R.D. O'Dea, H.M. Byrne, S.L. Waters, Continuum modelling of in vitro tissue engineering: A review, in: Studies in Mechanobiology, Tissue Engineering and Biomaterials, vol. 10, Springer, 2012, pp. 229–266.

[11] Greg Lemon, John R. King, Helen M. Byrne, Oliver E. Jensen, Kevin M. Shakesheff, Mathematical modelling of engineered tissue growth using a multiphase porous flow mixture theory, J. Math. Biol. 52 (5) (2006) 571–594.

[12] Greg Lemon, John R. King, Multiphase modelling of cell behaviour on artificial scaffolds: Effects of nutrient depletion and spatially nonuniform porosity, Math. Med. Biol. 24 (1) (2007) 57–83.

[13] Helen Byrne, Luigi Preziosi, Modelling solid tumour growth using the theory of mixtures, Math. Med. Biol. 20 (4) (2003) 341–366.

[14] Luigi Preziosi, Andrea Tosin, Multiphase modelling of tumour growth and extracellular matrix interaction: Mathematical tools and applications, J. Math. Biol. 58 (4–5) (2009) 625–656.

[15] Andrea Tosin, Luigi Preziosi, Multiphase modeling of tumor growth with matrix remodeling and fibrosis, Math. Comput. Modelling 52 (7–8) (2010) 969–976.

[16] M.E. Hubbard, H.M. Byrne, Multiphase modelling of vascular tumour growth in two spatial dimensions, J. Theoret. Biol. 316 (2013) 70–89.

[17] G. Sciumè, S. Shelton, W.G. Gray, C.T. Miller, F. Hussain, M. Ferrari, P. Decuzzi, B.A. Schrefler, A multiphase model for three-dimensional tumor growth, New J. Phys. 15 (35pp) (2013) 15005.

[18] R.J. Dyson, J.E.F. Green, J.P. Whiteley, H.M. Byrne, An investigation of the influence of extracellular matrix anisotropy and cell–matrix interactions on tissue architecture, J. Math. Biol. 72 (2016) 1775–1809.

[19] J.E.F. Green, J.P. Whiteley, J.M. Oliver, H.M. Byrne, S.L. Waters, Pattern formation in multiphase models of chemotactic cell aggregation, Math. Med. Biol. : J. IMA 35 (3) (2018) 319–346.

[20] K.J. Bayless, René Salazar, George E. Davis, RGD-dependent vacuolation and lumen formation observed during endothelial cell morphogenesis in three-dimensional fibrin matrices involves the alpha(v)beta(3) and alpha(5)beta(1) integrins, Am. J. Pathol. 156 (5) (2000) 1673–1683.

[21] Wonshill Koh, Amber N Stratman, Anastasia Sacharidou, George E Davis, In vitro three dimensional collagen matrix models of endothelial lumen formation during vasculogenesis and angiogenesis, in: Methods in Enzymology, vol. 443, 2008, pp. 83–101.

[22] Amber N. Stratman, W. Brian Saunders, Anastasia Sacharidou, Wonshill Koh, Kevin E. Fisher, David C. Zawieja, Michael J. Davis, George E. Davis, Endothelial cell lumen and vascular guidance tunnel formation requires MT1-MMP–dependent proteolysis in 3-dimensional collagen matrices, Blood 114 (2009) 237–247.

[23] Yaron J. Blinder, Alina Freiman, Noa Raindel, David J. Mooney, Shulamit Levenberg, Vasculogenic dynamics in 3D engineered tissue constructs, Sci. Rep. 5 (1) (2016) 17840.

[24] G. Serini, D. Ambrosi, E. Giraudo, A. Gamba, L. Preziosi, F. Bussolino, Modeling the early stages of vascular network assembly, Embo J. 22 (8) (2003) 1771–1779.

[25] Peter Carmeliet, Valérie Ferreira, Georg Breier, Saskla Pollefeyt, Lena Kieckens, Marina Gertsenstein, Michaela Fahrig, Ann Vandenhoeck, Kendraprasad Harpal, Carmen Eberhardt, Cathérine Declercq, Judy Pawling, Lieve Moons, Désiré Collen, Werner Risaut, Andras Nagy, Abnormal blood vessel development and lethality in embryos lacking a single VEGF Allele, Nature 380 (6573) (1996) 435–439.

[26] Napoleone Ferrara, Karen Carver-Moore, Helen Chen, Mary Dowd, Lucy Lu, K. Sue O'Shea, Lyn Powell-Braxton, Kenneth J. Hillan, Mark W. Moore, Heterozygous embryonic lethality induced by targeted inactivation of the VEGF gene, Nature 380 (1996) 439–442.

[27] Irmeli Barkefors, Sébastien Le Jan, Lars Jakobsson, Eduar Hejll, Gustav Carlson, Henrik Johansson, Jonas Jarvius, Won Park Jeong, Li Jeon Noo, Johan Kreuger, Endothelial cell migration in stable gradients of vascular endothelial growth factor a and fibroblast growth factor 2: Effects on chemotaxis and chemokinesis, J. Biol. Chem. 283 (20) (2008) 13905–13912.

[28] Pian Wu, Ya Fu, Kaiyong Cai, Regulation of the migration of endothelial cells by a gradient density of vascular endothelial growth factor, Colloids Surfaces B 123 (2014) 181–190.

[29] Bruce R. Zetter, Migration of capillary endothelial cells is stimulated by tumour-derived factors, Nature 285 (5759) (1980) 41–43.

[30] Elaine N. Unemori, Napoleone Ferrara, Eugene A. Bauer, Edward P. Amento, Vascular endothelial growth factor induces interstitial collagenase expression in human endothelial cells, J. Cell. Physiol. 153 (3) (1992) 557–562.

[31] Graziano Seghezzi, Sundeep Patel, Christine J. Ren, Anna Gualandris, Giuseppe Pintucci, Edith S. Robbins, Richard L. Shapiro, Aubrey C. Galloway, Daniel B. Rifkin, Paolo Mignatti, Fibroblast growth factor-2 (FGF-2) induces vascular endothelial growth factor (VEGF) expression in the endothelial cells of forming capillaries: An autocrine mechanism contributing to angiogenesis, J. Cell Biol. 141 (7) (1998) 1659–1673.

[32] Donny Hanjaya-Putra, Jane Yee, Doug Ceci, Rachel Truitt, Derek Yee, Sharon Gerecht, Vascular endothelial growth factor and substrate mechanics regulate in vitro tubulogenesis of endothelial progenitor cells, J. Cellular Mol. Med. 14 (10) (2010) 2436–2447.

[33] Gabriel Helmlinger, Mitsuhiro Endo, Napoleone Ferrara, Lynn Hlatky, Rakesh K. Jain, Growth factors: Formation of endothelial cell networks, Nature 405 (6783) (2000) 139–141.

[34] Papon Muangsanit, Victoria Roberton, Eleni Costa, James B. Phillips, Engineered aligned endothelial cell structures in tethered collagen hydrogels promote peripheral nerve regeneration, Acta Biomater. (2021).

[35] Lauren Macri, David Silverstein, Richard A.F. Clark, Growth factor binding to the pericellular matrix and its importance in tissue engineering, Adv. Drug Deliv. Rev. 59 (13) (2007) 1366–1381.

[36] Errol S Wijelath, Salman Rahman, Mayumi Namekata, Jacqueline Murray, Tomoaki Nishimura, Heparin-II domain of fibronectin is a vascular endothelial growth factor–binding domain, Circ. Res. 99 (2006) 853–860.

[37] Tom T. Chen, Alfonso Luque, Sunyoung Lee, Sean M. Anderson, Tatiana Segura, M. Luisa Iruela-Arispe, Anchorage of VEGF to the extracellular matrix conveys differential signaling responses to endothelial cells, J. Cell Biol. 188 (4) (2010) 595–609.

[38] Abha Sahni, Charles W. Francis, Washington Dc, Vascular endothelial growth factor binds to fibrinogen and fibrin and stimulates endothelial cell proliferation vascular endothelial growth factor binds to Fibrinogen and Fibrin and stimulates endothelial cell proliferation, Blood 96 (12) (2000) 3772–3778.

[39] Christiana Ruhrberg, Holger Gerhardt, Matthew Golding, Rose Watson, Sofia Ioannidou, Hajime Fujisawa, Christer Betsholtz, David T. Shima, Spatially restricted patterning cues provided by heparin-binding VEGF-a control blood vessel branching morphogenesis, Genes Dev. 16 (20) (2002) 2684–2698.

[40] Alvaro Köhn-Luque, W. de Back, Y. Yamaguchi, K. Yoshimura, M.A. Herrero, T. Miura, Dynamics of VEGF matrix-retention in vascular network patterning, Phys. Biol. 10 (6) (2013) 066007.

[41] A. Gamba, D. Ambrosi, A. Coniglio, A. de Candia, S. Di Talia, E. Giraudo, G. Serini, L. Preziosi, F. Bussolino, Percolation, morphogenesis, and Burgers dynamics in blood vessels formation, Phys. Rev. Lett. 90 (11) (2003) 118101.

[42] A. Tosin, D. Ambrosi, L. Preziosi, Mechanics and chemotaxis in the morphogenesis of vascular networks, Bull. Math. Biol. 68 (7) (2006) 1819–1836.

[43] D. Manoussaki, S.R. Lubkin, R.B. Vernon, J.D. Murray, A mechanical model for the formation of vascular networks in vitro, Acta Biotheoret. 44 (3–4) (1996) 271–282.

[44] Léone Tranqui, Philippe Tracqui, Mechanical signalling and angiogenesis. The integration of cell–extracellular matrix couplings, Comptes Rendus de l'Académie des Sciences - Series III - Sciences de la Vie 323 (1) (2000) 31–47.

[45] Patrick Namy, Jacques Ohayon, Philippe Tracqui, Critical conditions for pattern formation and in vitro tubulogenesis driven by cellular traction fields, J. Theoret. Biol. 227 (1) (2004) 103–120.

[46] R.D. O'Dea, S.L. Waters, H.M. Byrne, A multiphase model for tissue construct growth in a perfusion bioreactor, Math. Med. Biol. 27 (2) (2009) 95–127.

[47] Natalie J. Pearson, Rebecca J. Shipley, Sarah L. Waters, James M. Oliver, Multiphase modelling of the influence of fluid flow and chemical concentration on tissue growth in a hollow fibre membrane bioreactor, Math. Med. Biol. 31 (4) (2014) 393–430.

[48] Devang Odedra, Loraine L.Y. Chiu, Molly Shoichet, Milica Radisic, Endothelial cells guided by immobilized gradients of vascular endothelial growth factor on porous collagen scaffolds, Acta Biomater. 7 (8) (2011) 3027–3035.

[49] M.J. Holmes, B.D. Sleeman, A mathematical model of tumour angiogenesis incorporating cellular traction and viscoelastic effects, J. Theoret. Biol. 202 (2) (2000) 95–112.

[50] Papon Muangsanit, Aligned endothelial cell and Schwann cell structures in 3D hydrogels for peripheral nerve tissue engineering (Ph.D. thesis), University College London, 2019.

[51] C.L. Stokes, D.A. Lauffenburger, S.K. Williams, Migration of individual microvessel endothelial cells: Stochastic model and parameter measurement, J. Cell Sci. 99 (2) (1991) 419–430.

[52] M.A. Rupnick, C.L. Stokes, S.K. Williams, D.A. Lauffenburger, Quantitative analysis of random motility of human microvessel endothelial cells using a linear under-agarose assay, Lab. Invest. J. Tech. Methods Pathol. 59 (3) (1988) 363–372.

[53] A.R.A. Anderson, M.A.J. Chaplain, Continuous and discrete mathematical models of tumour-induced angiogenesis, Bull. Math. Biol. 60 (5) (1998) 857–899.

[54] Daniel A. Nunez, Experimental estimate of the diffusivity of Vascular Endothelial Growth Factor (Ph.D. thesis), Massachusetts Institute of Technology, 2006.

[55] Feilim Mac Gabhann, James W. Ji, Aleksander S. Popel, VEGF gradients, receptor activation, and sprout guidance in resting and exercising skeletal muscle, J. Appl. Physiol. 102 (2) (2007) 722–734.

[56] Alvaro Köhn-Luque, Walter de Back, Jörn Starruß, Andrea Mattiotti, Andreas Deutsch, José María Pérez-Pomares, Miguel A. Herrero, Early embryonic vascular patterning by matrix-mediated paracrine signalling: A mathematical model study, PLoS ONE 6 (9) (2011).

[57] Roeland M.H. Merks, James A. Glazier, Dynamic mechanisms of blood vessel growth, Nonlinearity 19 (1) (2006) C1–C10, arXiv:NIHMS150003.

[58] M. Nomura, S.I. Yamagishi, S.I. Harada, Y. Hayashi, T. Yamashima, J. Yamashita, H. Yamamoto, Possible participation of autocrine and paracrine vascular endothelial growth factors in hypoxia-induced proliferation of endothelial cells and pericytes, J. Biol. Chem. 270 (47) (1995) 28316–28324.

[59] R. Coy, G. Al-Badri, C. Kayal, C. O'Rourke, P.J. Kingham, J.B. Phillips, R.J. Shipley, Combining in silico and in vitro models to inform cell seeding strategies in tissue engineering, J. R. Soc. Interface 17 (164) (2020) 20190801.

[60] Jon Herman, Will Usher, SALib: An open-source Python library for sensitivity analysis, J. Open Source Softw. 2 (9) (2017) 97.

[61] Andrea Saltelli, Paola Annoni, Ivano Azzini, Francesca Campolongo, Marco Ratto, Stefano Tarantola, Variance based sensitivity analysis of model output. Design and estimator for the total sensitivity index, Comput. Phys. Comm. 181 (2) (2010) 259–270.

[62] Lester James V. Miranda, PySwarms: A research toolkit for particle swarm optimization in Python, J. Open Source Softw. 3 (21) (2018) 433.

[63] S.E. Bell, A. Mavila, R. Salazar, K.J. Bayless, S. Kanagala, S.A. Maxwell, G.E. Davis, Differential gene expression during capillary morphogenesis in 3D collagen matrices: regulated expression of genes involved in basement membrane matrix assembly, cell cycle progression, cellular differentiation and G-protein signaling, J. cell Sci. 114 (Pt 15) (2001) 2755–2773.

[64] Rakesh K. Jain, Molecular regulation of vessel maturation, Nat. Med. 9 (6) (2003) 685–693.

[65] Guoyuan Li, C. Rhett Jackson, Simple, accurate, and efficient revisions to MacCormack and Saulyev schemes: High peclet numbers, Appl. Math. Comput. 186 (1) (2007) 610–622.